UNIVERSITÀ DEGLI STUDI DI PADOVA

SCUOLA DI SCIENZE
Dipartimento di Geoscienze
Direttore Prof. Nicola Surian

TESI DI LAUREA MAGISTRALE IN GEOPHYSICS FOR NATURAL RISKS AND RESOURCES

SURFACE WAVES BACK-SCATTERING ANALYSIS OF SURFACE HETEROGENEITIES

Relatore: Dott.ssa Ilaria Barone
Correlatore: Dott. Claudio Strobbia

Laureando: Roger Puiggròs Valentines
Matricola: 2070914

ANNO ACCADEMICO 2023-2024

Dedicated to my grandparents

Contents

Abstract

The existence of heterogeneities within the near sub-surface becomes a potential hazard in subsurface exploitation activities. Consequently, accurately identifying and characterizing these discontinuities in seismic surveys is vital for effective threat mitigation. In this regard, investigating the back-scattering of surface waves generated by such obstacles emerges as a critical approach for locating and understanding these heterogeneities, thereby reducing potential risks.

This thesis focuses on analysing the presence of surface cracks of different sizes within synthetic homogeneous half-space models in 2D and 3D, together with a layered half-space model in 2D. Synthetic seismic data is generated for each model by numerically simulating the wave propagation using a staggered finite differences grid. These data is analysed with the data generated in models without heterogeneities in time and frequency domain.

Through the analysis of the back-scattering coefficient in frequency domain for the 2D models, a consistent behaviour of the phenomena is identified, and dimensionless expressions can be determined and related to other surface waves properties, which can be extrapolated to any type of crack and frequency studied.

Following, an analysis of 3D models over different frameworks is performed to identify the characteristics of scattering field which can become an important factor to locate and migrate near-surface heterogeneities on real data. Between them it has been identified the directivity of the scattering field, the location of the centre of the heterogeneity or the geometrical setting effects over the wavefield.

1. Introduction

1.1. Seismic methods for the subsurface characterisation

Seismic exploration methods are widely used in geophysical exploration to image and characterise the Earth's interior and the subsurface geological formations. These methods are based on the propagation of elastic waves in the Earth and the reflection and refraction of these due to the inhomogeneities in the Earth's velocity-density distribution (Sengbush, 1983).

In general, seismic methods are characterised by the following steps. Firstly, seismic waves are artificially generated from the surface or the near subsurface using different active sources, such as chemical explosions, air guns, vibroseis or weight drops. These waves propagate through the surface interior, and their propagation is influenced by the elastic properties and density of the materials the waves go through. Secondly, the response of the waves is detected at the surface using a set of receivers like geophones (land receivers) or hydrophones (marine receivers), spread at different distances from the source within the area of interest. These receivers are sensitive to the soil particle motion or pressure changes induced by the wave propagation. The data obtained is normally presented as a series of seismic traces, one for each receiver, called "seismogram". Thirdly, the data are processed in order to extract relevant information about the geological structures in the survey area.

To describe the paths that seismic waves experience, the analysis of wave propagation is done by using the geometrical ray theory used also in optics to describe light propagation, as in both cases the behaviour of waves is the same. Different seismic methods can be used depending on the size and depth of the targets.

The characterization of deep structures is obtained through the analysis of body wave reflections (Fig. 1), that happen at the interface between two media with different acoustic impedances, where the acoustic impedance is defined as the product of the medium density and the velocity of the wave (Lavergne, 1989). At these interfaces, part of the energy of the incident wave is transmitted to the second medium and the rest of energy is reflected back in the first medium. In reflection seismology, the information needed are primary wave reflections. However, this is only a part of the recorded data, thus some processing is needed. The processing sequence begins with noise removal, eliminating as much as possible any data unrelated to seismic reflections. Once the noise is largely removed and the resolution of

reflection data is increased, the final image is obtained by analysing the behaviour of the reflections at different receivers and migrate the data to locate the reflectors at their actual position.

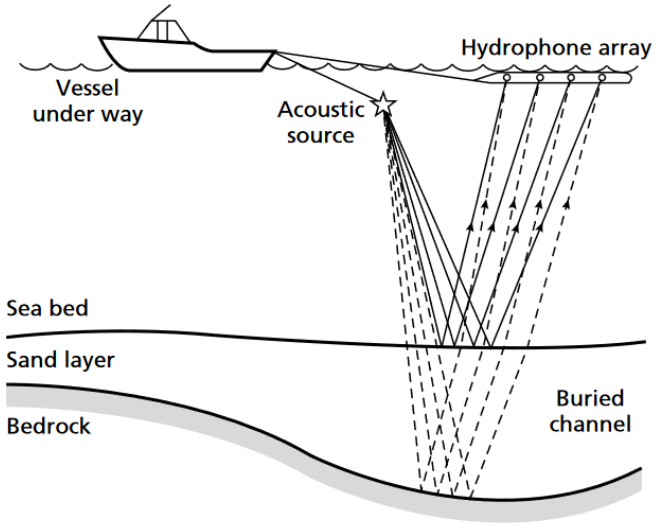

Figure 1: Schematic figure of the ray paths in seismic reflection in a marine survey. Figure from Kearey et al. (2002).

The behaviour of the reflected and the refracted waves is governed by the Fermat's Principle, which states that the wave path between two points will correspond to the one with least time propagation among all the possible paths. In a medium with constant velocity, this corresponds to a straight line (Burger et al., 2006). From this principle, Snell's Law is derived, describing wave behaviour at the interface between two layers, as shown in Fig. 2. In the reflection case, the incident angle (θ_i) and the reflected angle (θ_r) are equal with respect to the perpendicular vector to the surface between the two media ($\theta_i = \theta_r$). In the case of transmission, Snell's law is expressed as follows:

$$\frac{sin\theta_1}{v_1} = \frac{sin\theta_2}{v_2} \qquad (1)$$

where θ_1 and θ_2 are the angles of the incident and transmitted waves relative to the perpendicular vector to the boundary between the two media, and $v_1$and v_2 represent the velocities at which the waves travel within medium 1 and 2, respectively.

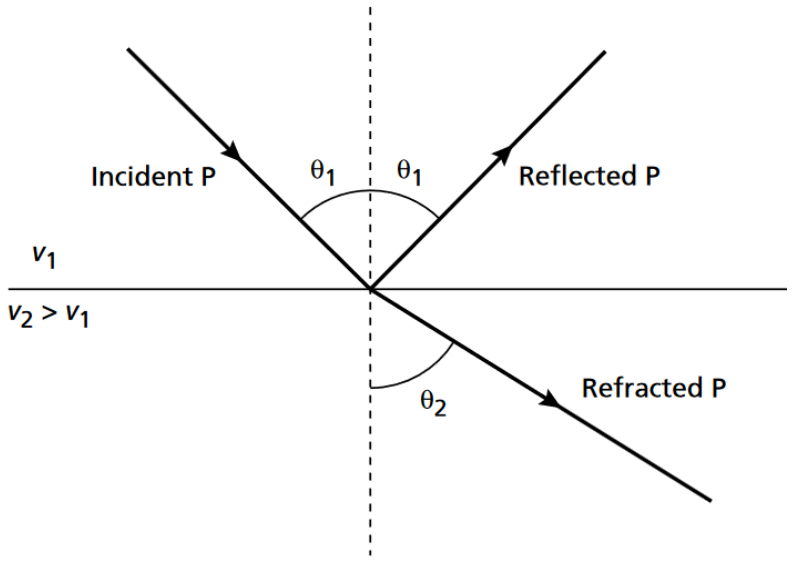

Figure 2: Reflected and refracted P-wave rays following Snell's Law produced by the interaction of an incident P-wave with an interface between two mediums with an acoustic impedance contrast. Figure from Kearey et al. (2002).

The amplitudes of the reflected and transmitted waves depend on the impedance values of the two media and the angle between the incident wave and the medium boundary. In the case of normal incidence, where the incident wave is perpendicular to the boundary, the reflection (R) and transmission (T) coefficients, describing the amplitudes of the reflected and of the transmitted waves with respect to the amplitude of the initial wave, respectively, are expressed by the following equations, where Z_1 and Z_2 are the acoustic impedance of the two media.

$$\begin{cases} R = \dfrac{Z_2 - Z_1}{Z_1 + Z_2} \\ T = 1 + R = \dfrac{2Z_2}{Z_1 + Z_2} \end{cases} \qquad (2)$$

As it can be seen, a larger acoustic impedance contrast will result in a higher value of the reflection coefficient and, consequently, in a stronger reflection.

The characterisation of the near surface is mainly obtained through the inversion of body waves refractions and/or through the analysis of surface waves. As for refractions, the main interest is on the characterization of waves' first arrivals, strictly related with critical refracted waves. This type of refracted waves occurs when the angle of the transmitted wave is 90

degrees. Over these circumstances, the generated transmitted wave travels along the boundary of the two media instead of being transmitted through the second medium. Mathematically, critical refraction behaviour is observed when the incident wave travels at an angle equal or bigger than the critical angle (i_c), described by the following expression derived from Eq. 1:

$$i_c = \sin^{-1}\left(\frac{v_1}{v_2}\right) \quad (3)$$

This expression indicates a critical condition for generating critical refracted waves at a layer boundary: the seismic velocity of the underlying layer, which is directly proportional to seismic impedance as defined previously, must exceed that of the upper boundary layer Failure to meet this condition results in the wave encountering a low-velocity layer, where the wave will not be critically refracted and instead it is transmitted to the second layer with an angle smaller than the one of the incident wave. According to Huygens' Principle, which states that all the points on a wave front can act as secondary sources of spherical wavelets (Burger et al., 2006), part of the energy will be critically refracted back to the surface, becoming the first arrival detected by receivers. Plotting the time of first arrivals against distance describes a curve shape comprising lines with diminishing slopes as distance increases, each line corresponding to the critical refracted arrivals coming from a different layer boundary (Fig. 3). These lines encode information of the layered system, specifically, the slope inversely correlates with the velocity of the undelaying layer while the depth of the upper layer can be retrieved from the intercept time of the line with the ordinate axis. Since seismic refraction method is blind to velocity inversions, the presence of a low velocity layer is interpreted as a single layer with pseudo depth and pseudo velocity values which are related to the actual depths and velocities of the two layers involved at the low-velocity boundary.

As for surface waves, they propagate along the interface between soil and air (or soil and water for the marine case), and they have a dispersive behaviour in a layered media (see section 1.2.2). Typically, the different techniques of surface wave analysis target the surface dispersion, from which it is possible to derive the shear-wave velocities of the near surface. Unlike the seismic refraction method, these techniques are capable of modelling low-velocity inversions (Socco et al., 2010). The surface waves analysis focuses only on the direct arrivals of surface waves. However, surface waves can be reflected and back-scattered when strong lateral heterogeneities are encountered, similarly to body waves. This thesis focuses on the

characterization, through numerical modelling, of the surface wave back-scattering, which carries important information about the near surface, and that is often neglected.

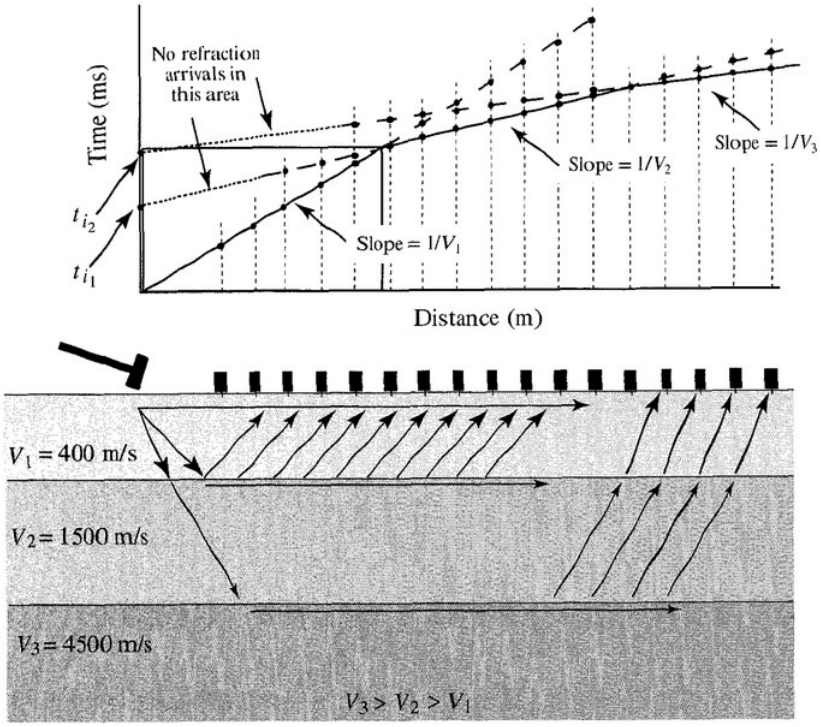

Figure 3: Figures illustrating the basics of refraction seismics. In the upper part, scheme of the time-distance curve of first arrivals for a three-layered half-space. Below, scheme of the ray paths of the first arrivals for a refraction seismics 2D survey in a three-layered half-space. Figure from Burger et al. (2006).

1.2. Types of seismic waves

Seismic waves are mechanical waves that propagate within and along the surface of the Earth or, in general, through any planetary body. These waves are radiated by natural or human sources and can be recorded by means of seismic sensors and recorders (Bormann et al., 2012).

Seismic waves are classified into two main types: body waves, which travel freely within the Earth propagating in all directions, and surface waves, which move bounded along the body surface. For that reason, surface waves are primarily used to study near surface structures, while body waves are used to study the structure of the interior of the Earth. Due to their

confinement to the near surface, surface waves have their energy concentrated in a smaller volume, leading to higher amplitudes in seismograms compared to body waves.

The most common natural generators of seismic waves are earthquakes, this phenomenon is characterised by a sudden release of energy stored in the Earth's crust due to the accumulation of stress. When this energy is released, it produces seismic waves that causes a sudden shaking of the ground when they propagate (T. Editors of Encyclopaedia, 2024). Several earthquakes occur daily, most of which are of very low magnitude. As the magnitude of an earthquake increases, its frequency of occurrence decreases. The frequency range of earthquakes typically falls between 0.001 to 4 Hz. These low frequency waves are detectable over considerable distances, especially in the case of largest earthquakes, which can produce seismic waves that circle the globe a number of times (Kennett, 2009).

Other main natural sources of seismic waves include landslides or volcanic related activity such as magma movement and eruptions. Also is notable mentioning the existence of other natural sources that produce very small frequency seismic waves, ranging in frequencies between 0.003 and 1 Hz. This sources that include tropical cyclones like hurricanes and typhoons. ocean waves or tornadoes, are characterised to be persistent in a scale that goes from hours to days (Tanimono et al., 2023). These types of sources are normally called seismic noise as their components are detected by the receivers, but its information is unwanted or not interpretable, and could lead to an incorrect interpretation of the data if not treated properly.

Seismic waves can also be generated by anthropogenic sources. Human-related seismic sources generally produce as persistent, low-energy and higher frequency signals, in comparison to natural sources. These sources can generate as seismic noise, and depending on the characteristics of the noise, such as its intensity or the distance from the recorder, the noise amplitudes can range from being barely detectable by seismograms to matching or even exceeding the magnitude of the signal. Seismic noise sources include vehicle traffic, construction work, and manufacturing activities. However, other anthropogenic sources can have a bigger footprint in seismograms and other seismic recorders in the lights of fireworks or "footquakes" from people jumping during sports or music events (Díaz et al., 2017), which can be detected in a range of kilometres or, in a bigger scale, mining explosions or nuclear tests (Stump, 1991) that can be detected in larger distances.

Of particular interest to geophysicists and seismologists are artificial sources such as chemical explosions, surface vibrators and weight-dropping devices which are related with seismic exploration. These sources are characterised by a short impulse source located in the surface or in the near subsurface, generating seismic waves with frequencies ranging between 5-100 Hz, depending on the type of source and its characteristics. The type of source and its dimensions also affect the investigation distances in which these sources can be detected and also the depth of penetration.

Weight drop sources can be detected at distances ranging from hundreds of meters to kilometres and obtain information up to the kilometre, approximately. Vibroseis can explore the subsoil to depths of several kilometres, depending on the dimensions of the vibroseis, and cover lateral distances up to tenths of kilometres. Chemical explosions range of exploration depends also on the quantity of explosive, but for huge amounts of explosive it can be explored in depth in the order of tenths of kilometres and distances on the order of tenths to hundreds of kilometres.

1.2.1. Body waves

Body waves are seismic waves that travel through the interior of the Earth propagating in nearly every direction (Båth, 1979). They are crucial for understanding the Earth's internal structure. There are two types of body waves, primary waves (P-waves) and secondary waves (S-waves). Their names reflect their velocity of propagation, with P-waves being significantly faster than S-waves and thus the first to be detected by seismic records, as seen in Fig. 4.

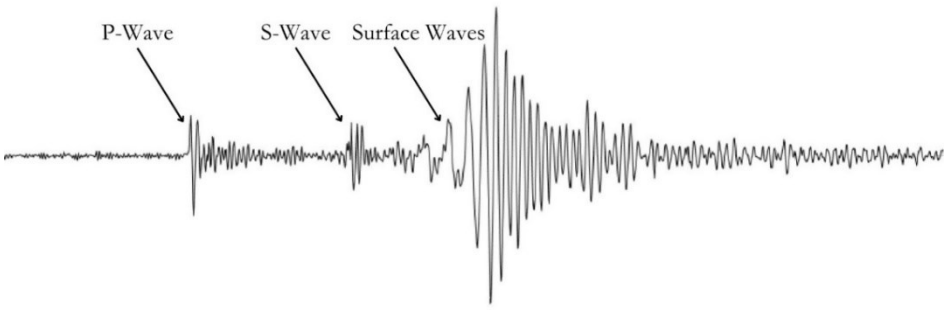

Figure 4: Seismogram showing the arrivals of the different types of seismic waves. Extracted from a M5.0 earthquake occurred on June 15,1995 near Jan Mayen Island (Norway). Modified from Schumaker (2006).

P-waves are also known as longitudinal waves, as they have a displacement that it is irrotational, occurring in the direction of the wave propagation, as shown in Figure 5a. During their propagation, P-waves introduce volume changes in the material, for that reason they are also called as compressional or dilatational waves (Shearer, 2009).

The motion of S-waves, as shown in Figure 5b, is perpendicular along the direction of propagation, earning them the names transverse or shear waves as, contrary to P-waves, this type of waves do not induce any volume changes in the media through they travel. Shear waves are divided into two components based on the plane in which the propagation vector lies. In the vertical plane perpendicular to the direction of propagation, shear waves are defined as SV waves, while the horizontal plane components are called SH waves (Shearer, 2009). The main difference between these components is that at the boundary between different media, incident SV waves can generate by refraction and reflection SV and P waves, and the same from incident P-waves. However, incident SH waves can only give rise to SH waves (Båth, 1979).

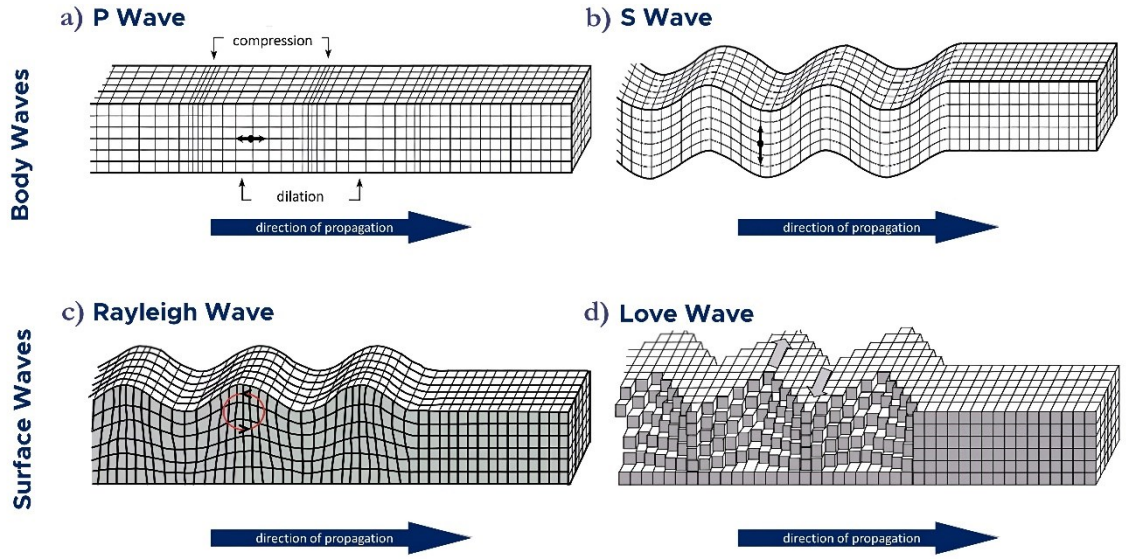

Figure 5: Schematic figures of the seismic wave propagation for the different types of seismic waves. a) longitudinal P-wave, b) shear S-wave, c) Rayleigh wave, d) Love wave. Modified form Bačić et al. (2020).

The velocity of propagation of body waves is related to the stiffness of the medium, which is influenced by factors such as composition, temperature, or pressure. And in linear elastic materials it is independent of the frequency (Foti et al., 2015). The velocities can be expressed in terms of the medium's density (ρ); the first Lamé parameter (λ), which, although does not

have a straightforward physical definition, it can be related to the medium's compressibility; and the second Lamé parameter (μ), also known as the shear modulus (G); as shown in the following expressions:

$$\begin{cases} v_p = \sqrt{\dfrac{\lambda + 2G}{\rho}} \\ v_s = \sqrt{\dfrac{G}{\rho}} \end{cases} \quad (4)$$

From these equations, it can be affirmed that velocity of propagation of P-waves is related to both Lamé parameters, while S-waves velocity only to the shear modulus. P-waves can propagate through any medium, but S-waves can just travel in solids because the shear modulus of fluids is zero.

Knowing that the shear modulus must be always positive, and that even if the first Lamé parameter can be theoretically negative, it is positive for all the most common rocks in Earth's crust and mantle in almost all conditions (Ji et al., 2010). From the physical expressions, it also can be seen that the velocity of the P-waves is always greater than that of S-waves. For example, for a Poisson solid (where $\lambda = G$), the ratio between the velocities is $\frac{v_p}{v_s} = \sqrt{3}$.

1.2.2. Surface waves

Surface waves are mechanical waves carrying elastic energy, generated by the presence of a free boundary (Foti et al., 2018), these waves emerge from the interaction of body waves at the interface of two mediums, such as the Earth's surface (Laske et al., 2015). There are various types of surface waves, distinguished by the propagation polarization of the ground motion, being Rayleigh and Love waves the most common.

First observed by Lord Rayleigh (1885), Rayleigh waves result from the combination of longitudinal (P) and vertically polarised transverse (SV) waves (Fig. 5c). They are characterised by an elliptical motion in the vertical plane along the direction of wave propagation (Foti et al., 2018). As shown in Fig. 6, the motion of surface waves near the surface is also retrograde (counterclockwise) due to the phase shift between P and SV waves

(Bormann et al., 2012). This retrograde motion persists down to a critical depth of approximately 0.2 times the wavelength, where the motion becomes completely vertical. Below this depth, the motion becomes prograde (clockwise), as the horizontal displacement becomes negative (Foti et al., 2015). Rayleigh waves are dominant in seismic records from surface sources as a significant portion of the energy generated is radiated in Rayleigh waves. In a homogeneous, linear elastic half-space, the value is approximately 67% of the energy generated. Also, Rayleigh waves are the only surface waves that can propagate along the free surface of a homogeneous medium (Socco et al., 2004).

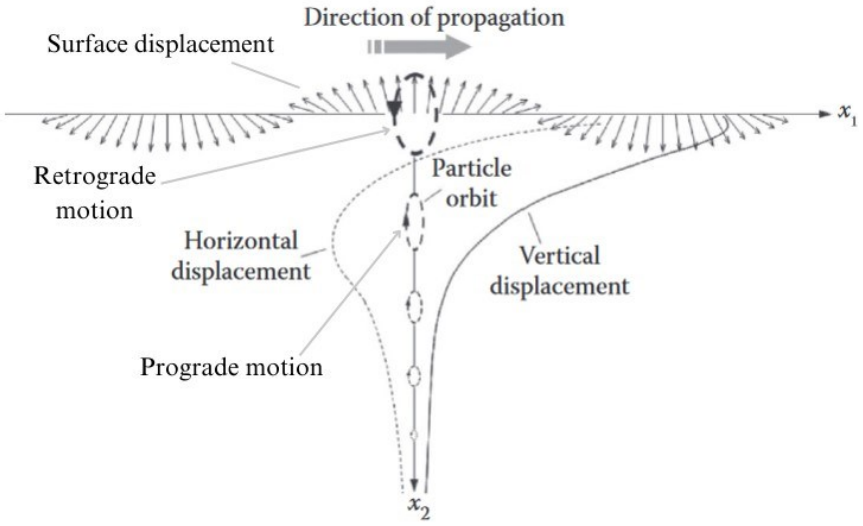

Figure 6: Rayleigh wave particle displacement and motion inside the first wavelength at depth. Image shows the curves of the displacements of the vertical and horizontal components with depth and the motion of the particle orbit, which is retrograde near surface and becomes prograde at a depth of approximately 0.2 wavelengths. Modified from Foti et al. (2015).

In heterogeneous media, another type of wave, known as Love waves, can also propagate. Predicted mathematically by A.E.H. Love (1911), Love waves arise from the repeated constructive interference of high-order, horizontally polarised transverse (SH) waves surface multiples at the free surface in an inhomogeneous medium (Shearer, 2009). Love waves exhibit transverse motion perpendicular to the direction of propagation in the horizontal plane, as seen in Fig. 5d.

Generally, surface waves can be considered as two-dimensional waves propagating along the surface they originate, as most of their energy is confined within a single wavelength unit, their amplitude decays very rapidly in depth (Rodriguez-Castellanos et al., 2007). Meaning that low-frequency surface waves, characterised by longer wavelengths, involve motion at greater depths compared to high-frequency waves, which remain confined to shallower regions.

In general, surface waves travel at lower velocities than body waves. Their velocity in a homogeneous media, which is independent of the frequency (Cook et al., 2001), is only determined by the material's Poisson ratio and wave shear velocity. Typically, surface waves velocities are defined between 5 and 13% slower than the ones of S-waves (Hess, 2002).

Another defining feature of surface waves is their dispersion nature in vertically heterogeneous media. Meaning that surface waves with different wavelengths travel at different velocities within such mediums. While these discrepancies in wavelength do not have a direct effect on the wave's velocity, as previously noted, they influence the depth of penetration (Fig. 7). Consequently, elastic properties encountered at different depths will be different, affecting the propagation velocity (Foti et al., 2018).

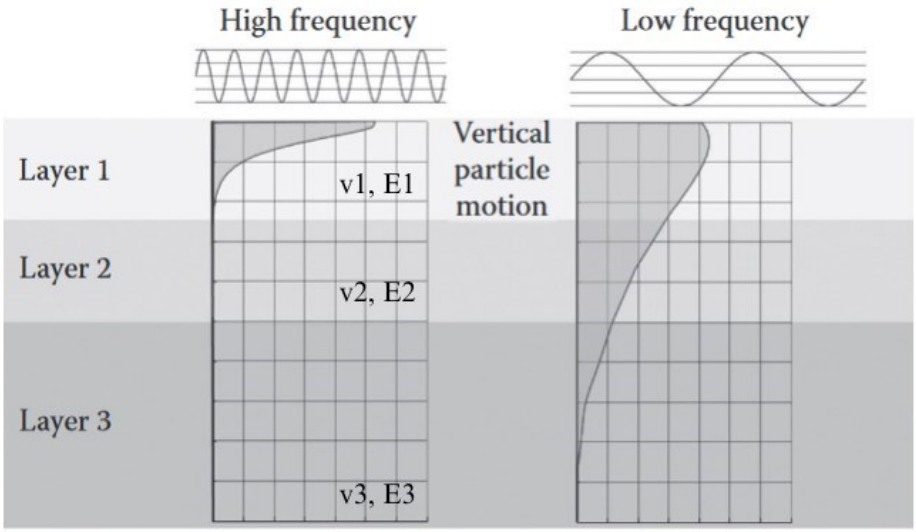

Figure 7: Scheme of the depth of penetration depending on the frequency, which influences the dispersion in layered media, as this depends on the elastic properties of the layer travelling. High frequency wave not present significant dispersion as it is enclosed within the first layer while the low frequency is affected by dispersion as encounters three different layers. Modified from Foti et al. (2015).

1.3. Wave scattering

Scattering is a fundamental physical phenomenon which describes the deviation and alteration of the motion of a particle or a wave as a result of an interaction due to the presence of other particles or non-uniformities, known as scatterers, within the medium through which it travels (Bohren et al., 1998). This interaction can result into a modification of the wavelength of the scattered entity compared to its initial state.

This phenomenon is found across several physical fields. Depending on the dimensions of the obstacle and the incident wave or particle, this interaction can be modelled differently and energetically categorised as either elastic or inelastic. Some common examples of scattering can be the red colour of the sky in sunsets in the electromagnetic field; in mechanics, the interaction of billiard balls; the collisions of particles inside particle accelerators in particle physics; or the nuclear interactions in a nuclear reactor in nuclear physics.

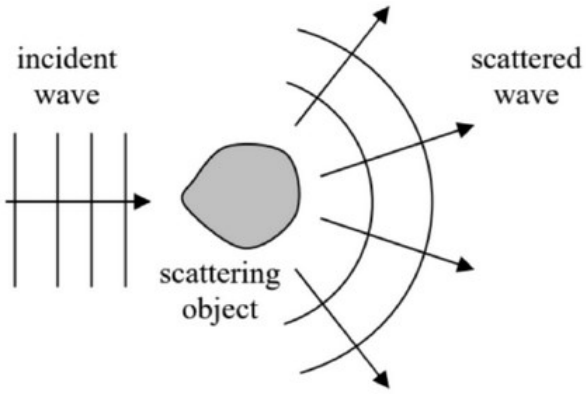

Figure 8: Wave scattering scheme. Figure from Likharev (2022)

In seismology, this effect is also significant and refers to the interaction of seismic wavefields with inhomogeneities in the subsoil (Shapiro et al., 1993) distorting the wave fronts and deflecting energy in all directions (Margerin, 2011). These irregularities can manifest across different scales, ranging from microscopic variations in the rock properties such as density or rock composition to macroscopic discontinuities within the Earth's crust, such as layer interfaces.

The study of scattering is crucial in seismology, as it contributes to the introduction of noise in seismic data obtained from earthquakes or seismic surveys, thereby impacting data quality.

Surface wave attenuation is another characteristic affected by scattering, along with absorption, especially in stratified mediums (Margerin, 2011). This results in a reduction of energy as wave fronts propagate away from the source.

Failure to adequately correct for these effects can lead to inaccuracies in imaging and interpreting subsurface structures or in seismic monitoring. Therefore, addressing scattering phenomena is imperative for ensuring the reliability and accuracy of seismic data analysis.

Furthermore, the presence of buried geological features such as shallow cavities or faults, which introduce lateral discontinuities in the subsoil, is another factor leading to the generation of a scattering field. The presence of this geological structures represents the main source of hazard during exploration and drilling. Wave scattering, more specifically near surface scattering (see paragraph 1.3.1), carries important information about the presence and location of these buried features. The identification and characterization of near surface scattering is therefore an important tool to mitigate the shallow geological hazards.

1.3.1. Near surface scattering

Waves propagating along elastic media can disturbed by the presence in the near surface of discontinuities such as faults, cracks, or cavities, among others (Johansen, 1967). When these heterogeneities are of similar size to the dominant wavelength of surface waves, these interactions induce the scattering of surface waves (Chai et al., 2014), leading to the generation of body waves, and reflected and transmitted surface waves (Achenbach et al, 1980).

Despite the generation of both types of waves, surface waves typically dominate in the scattering wave field in the near surface due to their smaller geometric attenuation ($\propto 1/\sqrt{r}$) compared to body waves ($\propto 1/r$), being r the distance from the source (Chai et al., 2012). Thus, body waves contribution become negligible at distances on the order of magnitude of one to two wavelengths from the source (Foti et al., 2015).

Mathematically, the total field resulting from the presence of scatters can be expressed as the sum of the incident field and the scattered field (Achenbach et al, 1981). Consequently, the scattered field can be conceptualised as a secondary source, its characteristics depending on those of the scatterers, such as the geometry or the depth (Mendelsohn et al., 1980). This

property renders the study of surface waves scattering a valuable method for locating scatterers at various scales across different fields.

Johansen (1967) delved into the study case of the scattering phenomenon generated by two semi-infinite planes joined by a step, using electromagnetic waves within a homogeneous half-space. The mathematical study has employed using the Wiener-Hopf technique leading to the obtention of satisfactory results in terms of the normalised transmission and reflection coefficients. The study was realised by considering both cases of initial incident wave travelling in the upper plane and in the lower plane.

In a similar vein, Munasinghe and Farnell (1973) employed a comparable setup to the previously described study but, in this case, focusing on the scattering produced by an incident Rayleigh wave. Their investigation involved a layered medium comprising an aluminium layer atop a semi-infinite fused quartz surface. To solve the problem, the authors used the finite difference method attaining results that closely aligned with analytical values for the dispersion curves. Both studies conclude that the scattering observed with an upward step is considerably higher than that of a downward step configuration.

The examination of the scattering indued by a surface crack in a homogeneous half-space utilizing Rayleigh surface waves is detailed by Achenbach et al. (1980). This investigation adopts a ray-theory approach, from which reflection, transmission and diffraction coefficients are used to characterize both back and front-scattering Rayleigh waves, along with elastodynamic stress-intensity factors. The approach showed to match results derived from various experimental and theoretical studies, especially when the wavelength has the same dimension or smaller than the crack depth.

Building upon the previous investigation, the same authors extended their research to encompass scattering phenomena using both incident surface and body waves within the same geometry (Mendelsohn et al., 1980). The study dissects the total scattered field into symmetric and antisymmetric fields in relation to the crack's plane. While the theory of the symmetric field corresponds to the one described in their preceding paper, the antisymmetric formulation is introduced within this paper. The problem is numerically solved after reducing the boundary-value problem into a singular integral equation, finding compelling results regarding the normalised back and forward-scattered fields with respect to the dimensionless frequency.

A third work was published by the same authors building upon the work already discussed, this time focusing on a geometry consisting of a sub-surface crack (Achenbach et al., 1981). They show that in the scattering observed in the far-field due to an incident Rayleigh wave, comprises scattered Rayleigh waves and body waves. Through plotting various coefficients against the dimensionless frequency relative to the distance from the surface of the top of the crack, as well as against the dimensionless crack position described as the ratio between the distance from the crack's top to the surface and the distance from the crack's bottom to the surface, the authors illustrate the different behaviours of the scattering field. These results demonstrate that as the ratio approaches zero, both the back-scattered effect and the stress-intensity factors increase, indicating that the majority of the energy, as theorised, propagates along the near-surface region.

In the frame of Non-Destructive Testing (NDT) techniques, Blake and Bond (1990) have presented a method grounded in a discrete mixed method based on finite element and finite difference methods. This approach produces stable and realistic solutions applicable to various geometries within a homogeneous half-space, including steps and wedges with diverse angles. For each scenario, the study presents the values of different coefficients associated with scattering, alongside computed synthetic seismograms, providing a comprehensive understanding of the method's applicability and efficacy across different structural configurations.

The wedge case is also explored by Budaev and Bogy (1995), where they introduce a numerical model based on the Sommerfeld's integrals to reduce the problem to a solvable, well-posed second order Fredholm integral equation. Rayleigh waves reflection and transmission coefficients due to the presence of an elastic free-traction wedge in a homogeneous half-space are computed as a function of the wedge's angle. Their model which shows results consistent literature values within a range spanning from 90º to 240º. However, this range is constrained by the limitations of the performance of a straightforward numerical analysis. To address this limitation, the authors refine their approach (Budaev et al., 1996), which enable them to increase the range of performance of the method. Their enhanced model demonstrates strong agreement with experimental data, encompassing angles ranging from 30º to 355º, thereby expanding the applicability and reliability of the method across a wider range of scenarios.

The investigation of a homogeneous half-space subjected to the influence of an incident Rayleigh wave under the presence of surface cracks or sub-surface cracks perpendicular to the surface is also visited in by Liu et al. (1996). In this case, the problem is constructed by a hybrid method in the frequency domain comprising two coupled regions. The first region, located over the crack space, describes the near-field scattering dynamics using the finite-difference method. In the second region, representing the far-field, the scattering field it is studied via the boundary integral representation described by Green's functions. Through an analysis of the normalised synthetic results across both time and frequency domains, enveloping surface displacements, crack opening displacements, and stress-intensity factors, the study reports that both superficial and sub-surface cracks can be identified and distinguished.

Riyanti and Herman (2005) developed a 3D elastodynamic surface wave dominant scattering study caused by the introduction of an incident P-wave over a two-layer, traction-free, elastic half-space housing a cube-like cavity in the near surface. Employing a numerical approach, the study tackles the problem through an integral-equation formulation involving the derivation of the Green's tensor. The results show the possibility to model 3D scattering problems in the near surface. Notably, the results unveil interference patterns and time-shifts resulting from the interaction between incident field and the surface waves. These interactions lead to a discontinuous and complex wavefield, offering insights into the dynamics of the near-surface scattering phenomena.

Exploring the scenario beyond surface-breaking cracks, Rodríguez-Castellanos et al. (2007) examine the scattering dynamics when multiple different cracks are present within a homogeneous half-space, under the influence of a Rayleigh wave as the incident wave. To tackle this numerical problem, the authors advocate for the utilization of the Indirect Boundary Element Method, which is based on the reduction of the diffracted field from the Somigliana's identity into an integral representation. The results, aligning with those from prior publications, focus on the Rayleigh wave amplification induced by the various cracks, with particular emphasis on the substantial amplification factor observed in the horizontal component. Furthermore, the study underscores the pivotal role of employing an accurate incident wave in both amplitude and direction. This precision is paramount for effectively discerning the presence of subsurface cracks.

Theoretical exploration of Rayleigh wave dynamics, influenced by scattering fields generated by the presence of heterogeneities within layered half spaces in presence of an incident wave containing body and surface waves is detailed by Chai et al. (2012). Employing the Betti-Rayleigh reciprocity theorem and the thin layer method, the study presents the discrete displacement expression. Furthermore, a numerical investigation is conducted, focusing on a simplified scenario involving a far field located near-surface rectangular cavity on a homogeneous half-space. The findings suggest that the back-scattering of Rayleigh waves is not only dependent upon the ratios of cavity depth and height relative to the wavelength but also correlated with the angular frequency. Notably, the study underscores that in the region above the cavity, wave behaviour aligns with the principles of guided waves in a free plate. Additionally, the study highlights the feasibility of estimating cavity face locations in cases of extended cavities where interference effects between near and far faces are minimal. This estimation is possible by analysing energy distribution and the "ripples" observed in the offset-wavelength domain.

In this work, near surface scattering is investigated through the generation of synthetic data. The geometry of the generated data mimics both 2D and 3D active seismic acquisition for exploration of natural resources. Data are generated from three SEG-Y files containing the information of the density, compressional, and shear velocities over the study model using Tesseral Pro software, which solves the elastic wave equation using the finite differences method on a staggered grid.

This work has the primary goal of characterising the scattering produced by near surface heterogeneities, and is propaedeutic to future studies, possibility of migrating the surface scattering and locating surface heterogeneities will be explored. In this study, surface cracks of different depths in homogeneous 2D and 3D half-spaces are analysed, along with a 2D study of a heterogeneous half-space. To fulfil the objective, an approach similar to that of Achenbach et al. (1980) and Mendelsohn et al. (1980) is followed to describe the back-scattering of waves by computing the back-scattering coefficient against different dimensionless parameters. Also, a 3D study is performed to understand the effect that different parameters have on the location and migration of heterogeneities, such study includes discussions on the directivity of the scattering field, the information obtained to locate the position of the crack, or the effects related to the geometrical setting of the study.

2. Methods

In this section the methods and analysis used to study the scattering field caused by the presence of heterogeneities are presented. First, the design and creation of various models will be described. Second, details of the data simulation process will be provided. Third, the methods used to analyse the scattering produced will be presented.

2.1 Model design and creation

To study the scattering produced by heterogeneities, some synthetic models are created to simulate wave propagation. These models, constructed on a dense grid of points, include the physical properties at each point. For an elastic model, these properties are compressional velocity (v_p), the shear velocity (v_s) and the density (ρ).

For each model, three SEG-Y files are required, each containing the information of one of the physical properties. In each SEG-Y file, the receiver trace coordinates correspond to the model position, the time axis of each trace correspond to depth, and the trace data represents the physical property at each coordinate and depth. In a 2D model, one of the two SEG-Y coordinates must remain constant, while in a 3D model, both coordinates vary.

2.1.1 2D models

The creation of 2D models must ensure the model is sufficiently long, with the crack far from the lateral borders, to study the scattering field produced by the crack at far offsets, where surface waves dominate over body waves.

It is also important to note that in a two-dimensional model it will always be defined as laterally infinite, so the scattered field produced by the heterogeneity will be along the vertical axis.

Designing these models requires creating multiple versions with varying crack sizes to study different scattering field behaviours. A reference model without any heterogeneity is also necessary for data processing and analysis. For consistency, all cracks are positioned at the same lateral location.

Several models have been created for this study, all measuring 1740 meters in length and 104 meters in depth, with the crack located 750 meters from the model's start. Two geological settings are used: a homogeneous half-space and a layered half-space. The homogeneous half-space is a simple one-layer model where surface waves do not undergo dispersion, with a compressional velocity of 800 m/s, shear velocity of 400 m/s, and density of 2400 kg/m³. The layered half-space consists of multiple horizontal layers, each with different physical properties, causing surface waves to disperse. This model features seven layers (Fig. 9) with specific parameters shown in Tab. 1.

	Vertical extension (m)	**Shear velocity (m/s)**	**Density (kg/m³)**
Layer 1	0 – 2.5	50	2400
Layer 2	2.5 - 5	90	2400
Layer 3	5 - 10	125	2400
Layer 4	10 - 20	200	2400
Layer 5	20 - 40	250	2500
Layer 6	40 – 70	350	2700
Layer 7	70 – 104	500	3000

Table 1: Physical properties of the different layers of the heterogeneous half-space.

The cracks introduced in each model are 1 meter wide and simulate the presence of air, with a density of 1 kg/m³ and velocities of v_p = 300 m/s and v_s = 5 m/s. For both half-space configurations, along with an initial model without a crack, models were built with crack sizes ranging from 2 to 80 meters, created at a depth interval of 2 meters. In the homogeneous study, models containing cracks of 1, 3, 5, 7 and 9 meters are also created to have a better understanding in the smaller cracks range.

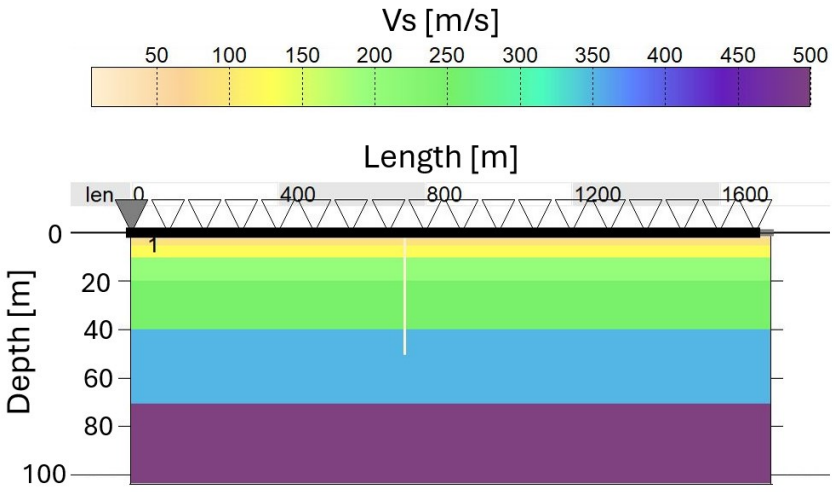

Figure 9: Scheme obtained from the Tesseral Pro software of the shear velocity data distribution for the case of a 50 meters crack in a layered half-space.

2.1.2 3D models

The design considerations for a 3D model are similar to the 2D case. The crack must be away from the model's borders to study the far field effects, but the model should not be excessively large to avoid high computational costs. Therefore, 3D models with dimensions of 292 meters inline, 216 meters crossline starting from coordinate (100, 100), and 140 meters deep are chosen. The finite crack, intended to study waves scattered from its sides and bottom, is located at 138 meters inline and spans from 153.25 to 227.50 meters crossline.

In total, three different homogeneous models with the same physical properties as the 2D homogeneous half-space have been created. The first model is crack-free, while the other two have cracks that are 1-meter wide and with depths of 14 and 60 meters.

2.2 Full waveform data simulation

Once the models are created, to obtain the synthetic seismic data, a full waveform simulation is produced by using the software Tesseral Pro, developed by TESSERAL Technologies. This software allows a highly accurate wave field modelling, in both 2D and 3D, based on the introduction of a source pulse on an introduced model using a defined set of sources and receivers.

2.2.1 Finite differences method

To produce the full waveform simulation, the software employs a computational scheme based on the finite difference method to solve the elastic wave equation. This numerical technique approximates solutions to differential equations by replacing continuous derivatives with discrete differences. This method is particularly useful for solving partial differential equations (PDEs), such as the wave equation, when analytical solutions are difficult or impossible to obtain.

To do that, Tesseral Pro discretises the model domain into a grid or mesh, where the derivatives at each grid point are iteratively approximated at each time step by using the 2nd order central finite difference method, which solves the function using the values of adjacent points in the previous time step.

The mesh in this case is constructed by a staggered grid, where velocity and stress values are defined in different points, which permits the improvement of the accuracy of the numerical method without increasing the computational needs. More information of how the elastic wave equation is solved using this numerical method is provided in Appendices 1.1 and 1.2 for the 1D and 2D cases, respectively.

2.2.2 Computation parameters: Model stability

Stability is a crucial aspect of any numerical method, determining whether the numerical solution to a differential equation converges to the true solution as the grid is refined. In other words, a stable finite difference scheme ensures that errors, whether arising from initial conditions, boundary conditions, or numerical approximations, do not grow uncontrollably as the computation proceeds.

In the case of the finite differences method, the numerical stability is not ensured even using an implicit method, as the stability is controlled by the computation grid parameters. If they are too big, the numerical simulation will be instable producing a different solution from the real one.

In the case if seismic model generation, the grid parameters are the sampling rate and the grid spacing. The sampling rate is defined as the number of discrete samples taken of a waveform per second, therefore it controls the time distance between two-time steps (Δt).

On the other hand, the grid spacing (Δd) is defined as the distance between two adjacent grid points. Although this parameter can be defined differently for each spatial direction, in Tesseral Pro it remains constant.

In order to ensure numerical stability two conditions have to be fulfilled. These conditions show in Eq. 5, have been derived and explained in Appendix 1.3. The first condition is obtained from the Von Neumann stability analysis, while the second condition is necessary to avoid numerical dispersion (Mufti, 1990). At the first condition, parameter *a* depends on the dimensions of the model, for a 2D case the parameter value corresponds to *a=2*, while in 3D *a=3*. Regarding the other parameters, c_{max} and c_{min} are the minimum and maximum velocities found in the model and w corresponds to the number of wavelength samples for the maximum frequency, which in general is defined as $w \geq 10$.

$$\begin{cases} \Delta t \leq \dfrac{\Delta d}{\sqrt{a}\, c_{max}} \\ \Delta d \leq \dfrac{c_{min}}{w\, f_{max}} \end{cases} \quad (5)$$

In this thesis, the simulations are performed using a time step of 0.5 milliseconds and a grid spacing of 0.5 meters for the 2D case, while for the 3D case, a time step of 0.35 milliseconds and a grid spacing of 1 meter where used. This bigger grid spacing on the 3D model compared to the 2D cases, is chosen as it reduces to half the quantity of points where the wave equation has to be solved, saving a considerable amount of time and computation resources. Meanwhile, the decrease of the time step in the 3D model is related to the increase of the value of the parameter a.

2.2.3 Source pulse

Another important parameter to be defined in the simulation is the source pulse. The source simulates the wavelet produced by the seismic source and it is the initial condition for the simulation.

In this thesis, a Ricker wavelet, also known as the Mexican hat wavelet due to its shape in the time domain, has been used (Fig. 10). In the frequency domain, as seen in the same figure, this wavelet is centred around a defined frequency where its amplitude is maximal, decreasing as the frequency moves away from the centre frequency.

The Ricker wavelet used in the simulations has only a vertical component, reflecting typical real-world conditions. The surface of the model is defined with a free boundary condition, allowing the deformation induced by the wave propagation.

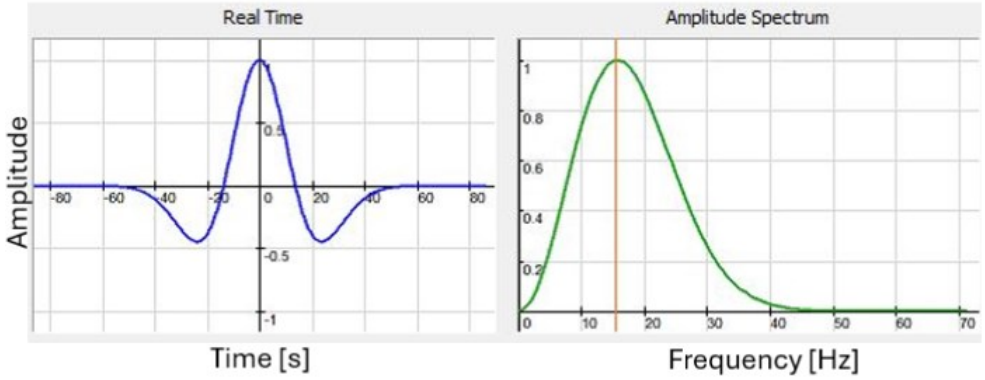

Figure 10: Scheme obtained from the Tesseral Pro software where it is shown the amplitude of a 16 Hz Ricker wavelet in time domain (left) and in frequency domain (right).

2.2.4 Recording configuration

The final aspect to configure for the simulation is the recording setup, as in a real seismic survey. This involves defining the positions of shots and receivers. To fully understand the scattering in the entire model, hundreds of receivers can be placed on the model surface, given there are no physical constraints. The only constraint to be considered is that the spacing between two shots or receivers must be greater than the grid spacing defined in the simulation, as no different information can be obtained under that threshold.

For the 2D case, shots are located every 100 meters, while receivers are spaced every 2 meters and remain active for all shots. For the 3D cases, shots and receivers are positioned both inline and crossline every 50 and 2 meters, respectively (Fig. 11).

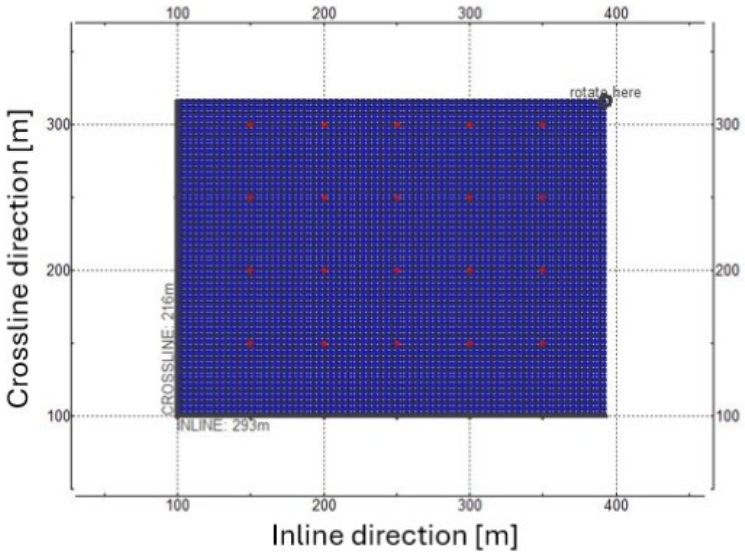

Figure 11: Scheme obtained from the Tesseral Pro software where it is shown the spatial distribution of shots (red dots) and receivers (blue dots) over the hole model.

2.3 Scattering analysis

Upon completion of the simulation, synthetic shot gathers are created at each receiver for x, y, and z directions, as well as pressure. This seismic data can then be analysed to understand the scattering field behaviour using various methods in both the time and frequency domains.

2.3.1 Effects of the heterogeneities

The starting point for analysing the scattering produced is to understand how the different waves interact with the heterogeneity. To show that, data can be directly displayed in shot gathers, which is the format obtained as a result of the simulation.

2.3.1.1 2D reflections and conversions

Fig. 12 shows as an example of the shot gather obtained on a 2D layered model for both inline and vertical components. As it can be observed the waves are dispersive as expected for a layered model.

Focusing on the effects produced by the scatterer, reflections are primarily observed at trace number 376, corresponding to a distance of 750 meters, the scatter location. Analysing these reflections reveals two types of reflected waves appear from the surface waves reflection. The more energetic reflections have the same slope of the incident surface waves, indicating reflected surface waves. However, a second type of wave, with a higher velocity, suggests that some of the reflected waves have been converted into body waves.

This behaviour is also found for the body waves, where reflected body waves are observed together with reflected waves that have been converted to surface waves.

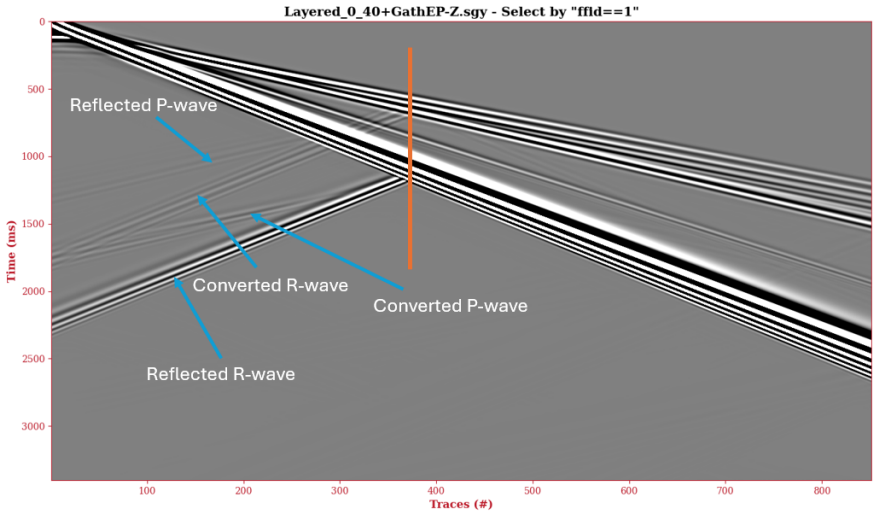

Figure 12: Shot gathers produced by a 40-meter crack in a 2D layered model. Incident body and surface waves are located together with the reflected and the converted surface and body waves. The scatterer position, at 750 meters, is located with an orange line.

2.3.1.2 3D reflections, diffractions and conversions

Continuing with the analysis for a 3D model, horizontal slice of the shot gather perpendicular to the heterogeneity (Fig. 13) clearly shows reflections and conversions of surface and body waves, similar to the 2D model.

Another method to investigate the wave propagation in the 3D model is by taking a snapshot of the amplitudes for all the receivers at a certain time. As illustrated in Fig. 14, this method reveals the presence of diffractions at the borders of the crack due to its finite size.

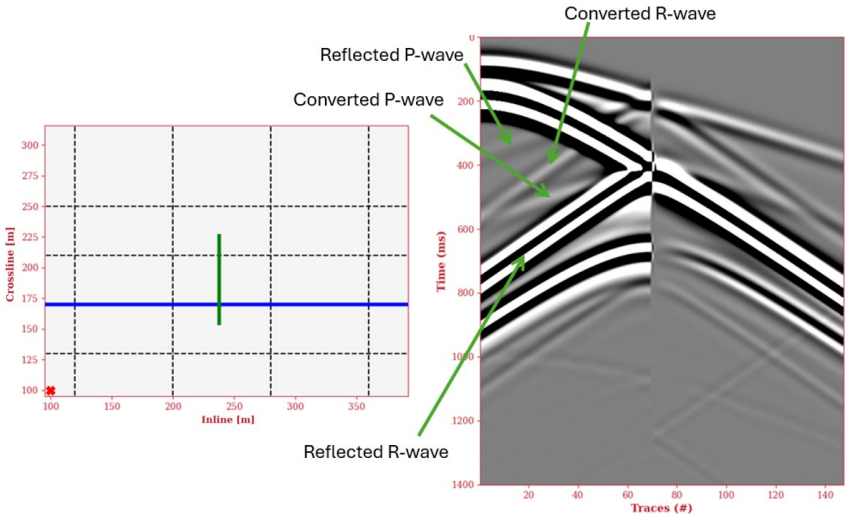

Figure 13: On the left, scheme of the 3D model in surface, locating the shot position (red cross), the crack position (green line) and the 2D line (blue line), which its shot gather is shown on the right, together with the location of the reflected and converted body and surface waves.

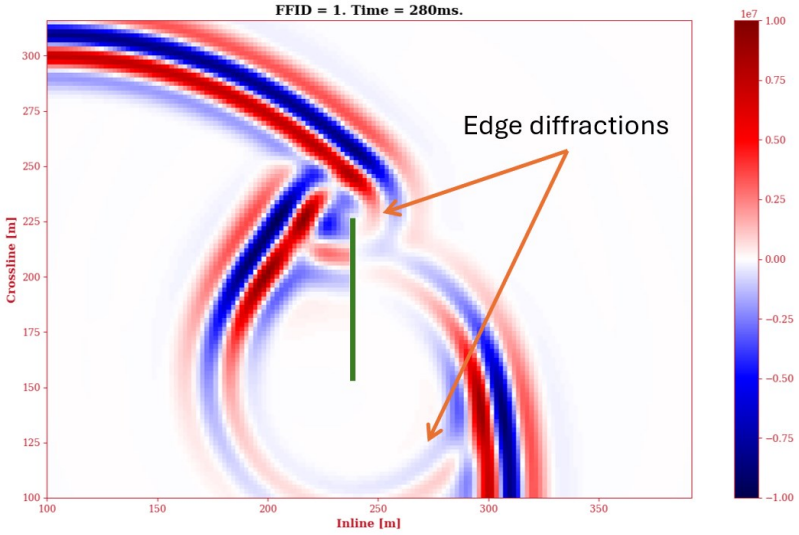

Figure 14: Time snapshot of the amplitude distribution in space for a 16-meter crack on a 3D homogeneous model showing the diffractions produced at the edges of the crack.

2.3.2 Extraction of the scattering field

The scattering field can be extracted and isolated. In order to do it, the description of the total field as the sum of the incident field and the scattered field can be used (Achenbach et al, 1981). This is the reason for creating that the models without cracks, as by subtracting the

amplitudes of the field without cracks (Fig. 15), acting as the incident field, from the total field (Fig. 16), the scattering field it can be obtained an isolated (Fig. 17). Looking into it, the reflexions and conversions explained in the previous section, can even be observed more clearly.

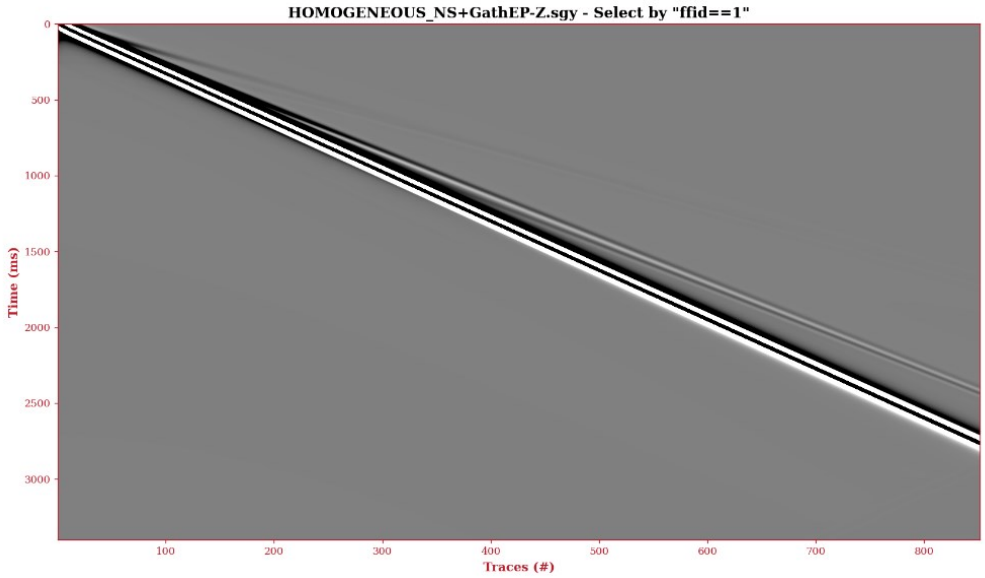

Figure 15: Raw shot gathers for a 2D homogeneous half-space without any crack produced by a 16 Hz Ricker pulse.

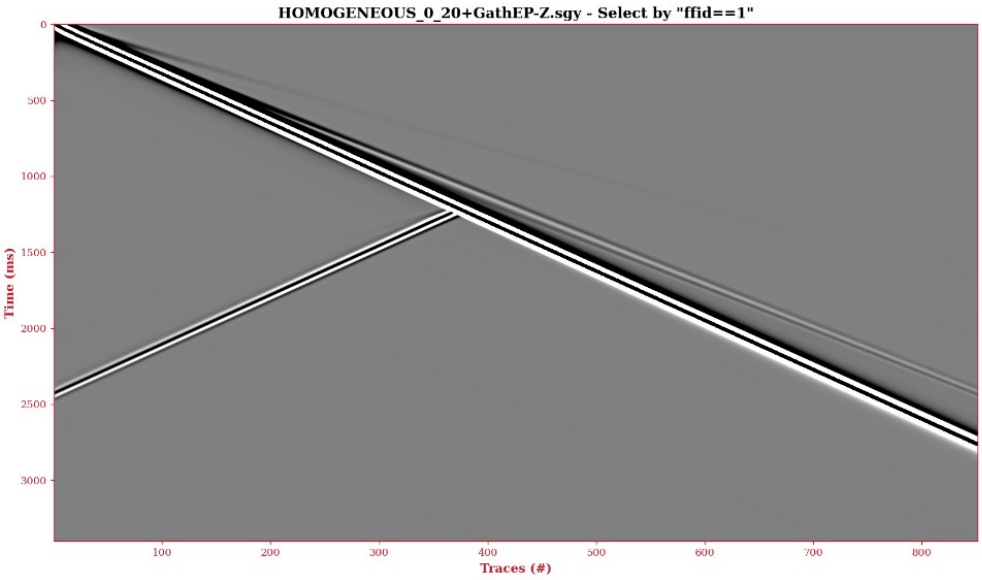

Figure 16: Synthetic seismogram obtained by the presence of a 20-meter depth, 1meter wide superficial crack, in a homogeneous half-space produced by a 16 Hz Ricker pulse.

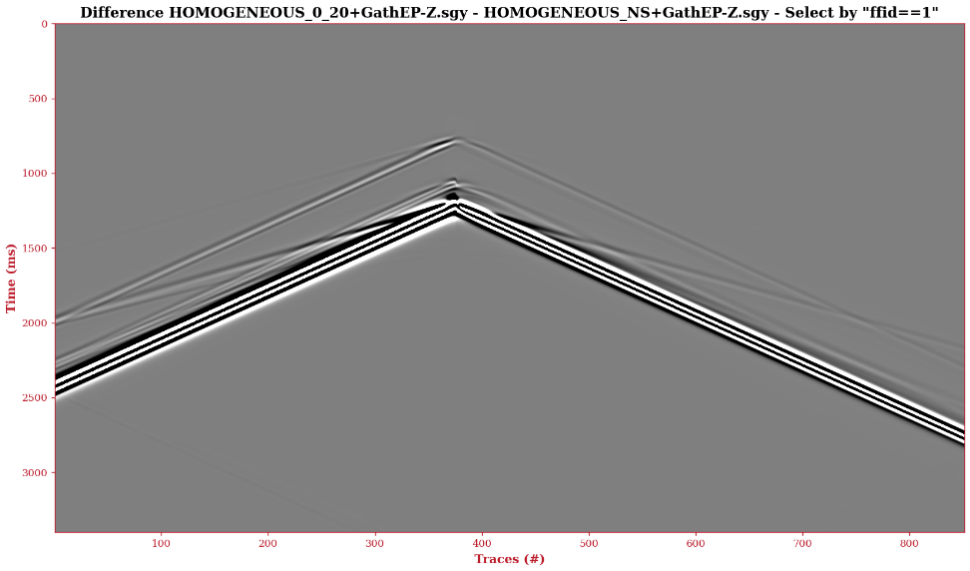

Figure 17: Scattering shot gather obtained for a 2D homogeneous half-space with a surface crack of 40 meters obtained by subtracting the data from the model without any crack and the 20 meters crack model. Both models produced by a 16 Hz Ricker pulse.

2.3.3 Spectral analysis

Once the scattering information has been extracted and studied in time domain, data can be transformed employing a discrete Fourier Transform into the frequency domain to realise a spectral study. The same process is applied to the raw data of the model containing no heterogeneities for further studies (Fig. 18). As it can be seen in Fig. 19, the scattering field is stronger on the back-scattering side as the amplitudes in frequency domain are higher than in the forward side. Also, it can be observed that the peak values are observed at frequencies near the frequency used in the initial Ricker pulse.

2.3.4 Geometric dispersion correction

In order to compare results between the scattering field and the incident field some corrections need to be done in order to obtain meaningful results. One of these corrections to be considered is due to the geometric divergent nature of seismic waves, which results in greater attenuation of back-scattered waves. This attenuation occurs because the back-scattered waves have travelled a greater distance compared to the incident wave at the same offset position.

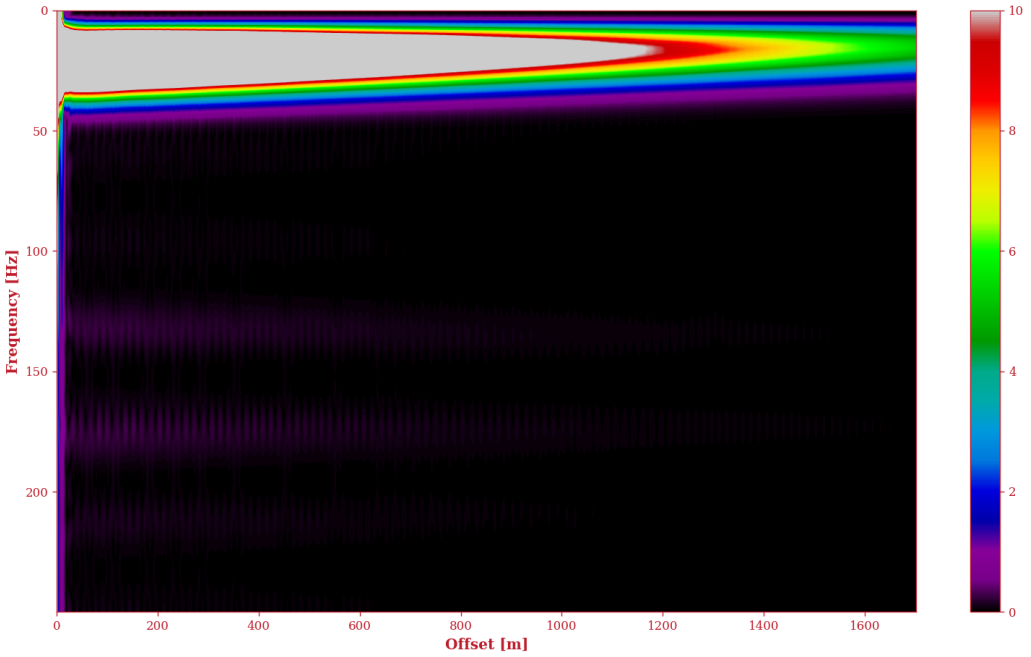

Figure 18: Frequency domain spectra against the offset (in meters) of the non-scattered case using a 16 Hz Ricker pulse.

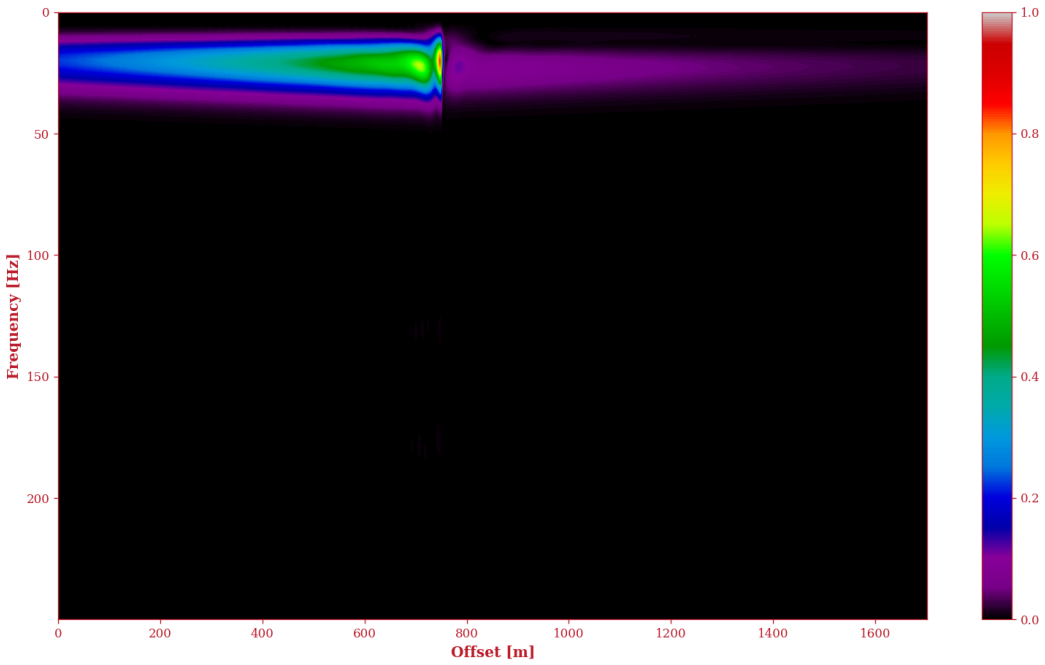

Figure 19: Frequency domain spectra against the offset (in meters) of the scattered field produced by a 20-meter crack by using a 16 Hz Ricker pulse.

Therefore, as the energy is distributed over a larger area, the local energy density is smaller, as this magnitude is inversely proportional to the radius. In this case as the energy is back-scattered the radius can be interpreted as the distance travelled. To be precise, the additional distance travelled corresponds to twice the offset distance from the crack position.

This physical phenomenon can be addressed through various methods such as the use of a gain function. However, in this particular case, the values of the scattering are compared to the value at the incident field (model without crack) at the point where the distance travelled is equal to the one done by the back-scattered wave.

2.3.4.1 2D correction

In the case of a two-dimensional model this position corresponds to the mirrored position of the back-scattering offset relative to the crack location. Remarkably, this mirrored position also lies at a distance equivalent to the additional distance travelled by the back-scattered waves, as shown in Fig. 20. Consequently, both scenarios experience identical attenuation, eliminating the necessity for correction due to attenuation phenomena.

This correction can be done this way as in the computation of the synthetic data it has been obtained considering no intrinsic attenuation on the half-space due to friction and lateral heterogeneities, apart from the main heterogeneity which produces the back-scattered field. Making geometric divergence the only factor involved in the decrease of energy amplitudes with distance.

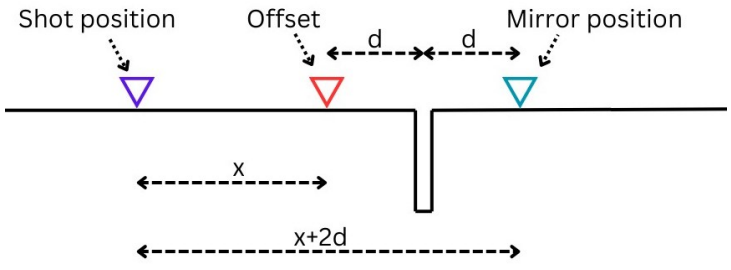

Figure 20: Schematic diagram of the distances between the positions and distances between the shot, the receiver position, the crack location, and the mirror position of the receiver to the crack.

2.3.4.2 3D correction

When designing the 3D models, as well as for the 2D case, it has been considered no intrinsic attenuation on the half-space due to friction and lateral heterogeneities, so the attenuation is purely geometrical.

To properly correct for the geometrical displacement in a 3D model, it is assumed that the main scattering is produced at the nearest edge of the scatterer in relation to the shot location, as shown in Fig. 21 as the sum of d1 and d2. For that reason, the scattering distance (*d*) travelled from the source to the receiver can be expressed a shown in Eq.6.

$$d = \sqrt{(x_{shot} - x_{sca})^2 + (y_{shot} - y_{sca})^2} + \sqrt{(x_{sca} - x_{rec})^2 + (y_{sca} - y_{rec})^2} \quad (6)$$

Where, *x* and *y* represent the cartesian coordinates of the shot position (*shot*), the nearest edge of the scatterer (*sca*) and the study position (*rec*).

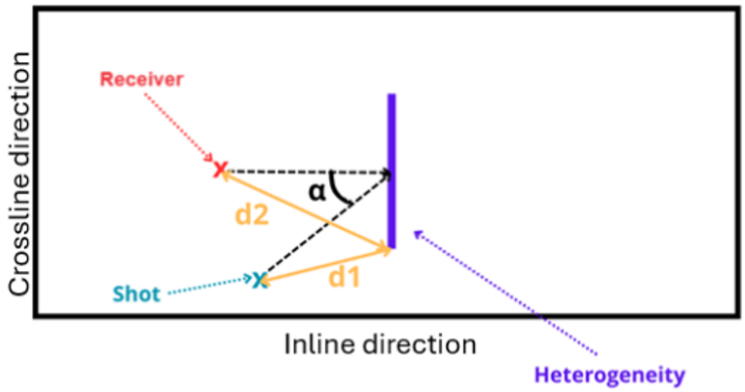

Figure 21: Scheme of the surface of the 3D model viewed from above, where the scattering distance d *is defined as the sum of* d1 *and* d2.

As in a three-dimensional model the geometrical attenuation in all directions is the same, the "mirror" position to be compared with the back-scattering studied can be any point at a radius *d* from the source. Taking advantage of this factor, the mirror position is defined as the inline position to the shot (same vertical value) at a distance *d*.

2.4 Displacement of surface waves with depth

The displacements produced by a surface wave vary with depth, and their profile can be obtained by computing the eigenfunction of the fundamental mode of the surface wave.

Fig. 22 shows the normalised eigenfunction for the homogeneous half-space case for a frequency of 16 Hz. The vertical component eigenfunction shows an amplitude peak in the near surface, followed by a rapid amplitude decay until the displacement reaches null around 1.5 times the wavelength of the surface wave ($\lambda \approx 23.3$ meters in this case). This behaviour is consistent across the different frequencies with variations at the depths of the amplitude peak and the zero-amplitude points related with the frequency.

For instance, as shown in Fig. 23 for a 6 Hz wave in comparison to the 16 Hz case, lower frequencies exhibit amplitude peaks and zero-amplitude depths at greater depths compared to higher frequencies.

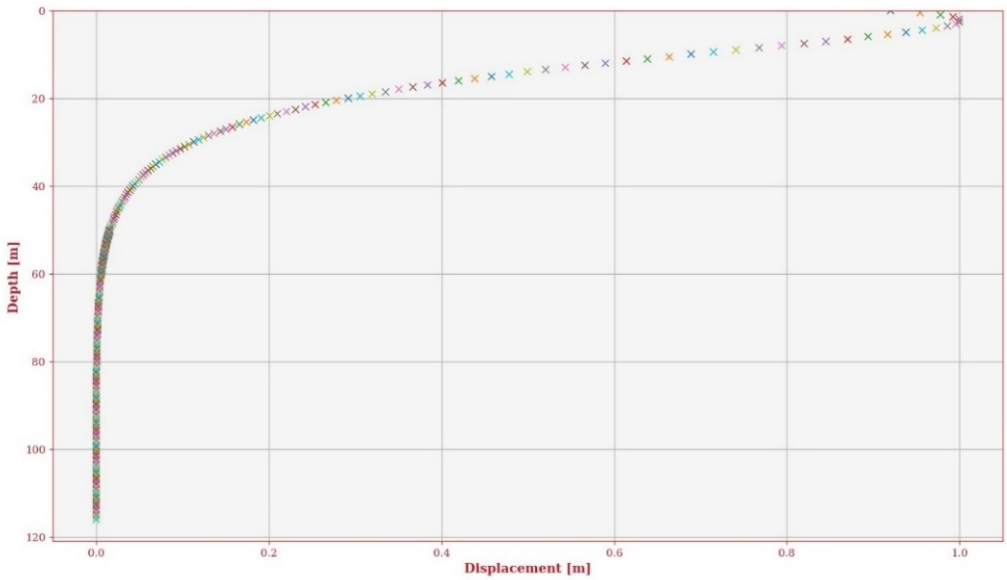

Figure 22: Normalised surface wave vertical component eigenfunction for a 16 Hz wave in a homogeneous half-space.

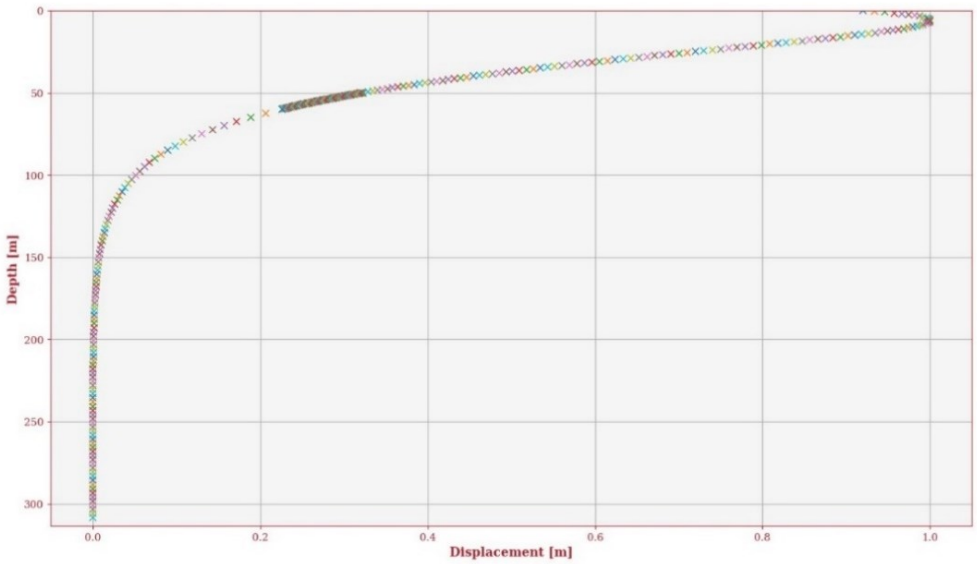

Figure 23: Normalised surface wave vertical component eigenfunction for a 6 Hz wave in a homogeneous half-space.

2.4.1 Cumulative energy integration

The energy of surface waves predominantly concentrates near the surface, with its magnitude related with the square of the displacements (Feynman et al., 1965). From the vertical component eigenfunction, the plot of the cumulative energy with depth can be derived, indicating the percentage of surface wave energy enclosed between the surface and a specific depth.

To derive this magnitude, the eigenfunction amplitudes are initially squared, as energy can be interpreted as the integral beneath the squared eigenfunction curve. Subsequently, discrete cumulative integration is performed to determine the energy situated between the depth of a given point and the surface.

For integrating under a set of discrete points, the cumulative trapezoid method is utilised. This method employs the trapezoidal numerical technique to approximate the definite integration between two points through the following expression:

$$\int_a^b f(x)dx \approx (b-a) \cdot \frac{f(a)+f(b)}{2} \quad (7)$$

Here, *a* and *b* represent two discrete points, while *f(a)* and *f(b)* denote the values of the function analysed at these points. Finally, to derive the cumulative integral value, the result of the integral between the two points is added to the sum of all the discrete integrals between points at shallower depths.

Mathematically, the cumulative energy at a certain depth ($E(z_N)$) can be expressed by the following expression:

$$E(z_N) = \sum_{k=1}^{N} (z_k - z_{k-1}) \cdot \frac{\delta(x_{k-1})^2 + \delta(x_k)^2}{2} \quad (8)$$

Where, z_k represents the depth of a particular discrete point, and $\delta(x_k)$ denotes the displacement at that point.

3. Results

This chapter will describe the results derived from the methods presented in the previous chapter. Initially, a study of the 2D models is performed over a dimensionless parameter to study the scattering field produced by a crack. Following, a study over the 3D models is presented to understand how scattering behave in three dimensions on different frameworks. Finally, the computation of the energy distribution with depth for a surface wave is presented.

3.1 Dimensionless relation of the scattering field: Back-scattering coefficient

In order to derive meaningful results, the use of a dimensionless relation can lead to the generalisation of the results obtained. Focusing in the 2-dimensional models the main objective is to study the scattering field behaviour as a function of the crack size. Taking this into advantage and to study if the behaviour is also the same for any frequency, the results can be plotted against the dimensionless ratio between the crack size and the wavelength related to the studying frequency.

As the final purpose of this thesis is to obtain the suitable information to study the possibility to locate and migrate heterogeneities in real data the property of the scattering field studied is the back-scattering field. This choice is because in general heterogeneities will be located outside the line of receivers. Although some information for the forward-scattering can be obtained in a 3D study if the heterogeneity is located inside the zone of receivers, in general, the information that can be retrieved in both 2D and 3D surveys is the information of the back-scattering field.

To quantify the back-scattering energy resulting from the presence of a crack, the concept of back-scattering coefficient is defined. This coefficient represents the ratio of the amplitude, in the frequency domain, of the back-scattering energy to the amplitude at the same position and frequency for the incident wave.

To compute the back-scattering coefficient, once the synthetic seismic data is generated, initially the scattering field is obtained by proceeding as described in Section 2.3.2. At the time the scattering field is retrieved, this together with the seismic data for the case without scattering undergo the spectral analysis (Section 2.3.3) where the back-scattering field is

computed after correcting the geometric dispersion by taking the incident wave amplitude at the mirror position (Section 2.3.4).

3.1.1 Homogeneous case

Before computing the back-scattering coefficient for the 2D homogeneous it is essential to acknowledge an effect to be corrected in order to be able to compare the results at different frequencies. The spectral ratio between the scattering and the input wavefield gives the amplitude ratio for a specific frequency part of the consider wave train, considering the ratio of the event, the number of cycles increases with the frequency, for that reason the ratio has to be normalised to obtain an energy estimation consistent for all the frequencies.

Mathematically, the computation of the back-scattering coefficient (*BC*) for one frequency can be described by the following expression:

$$BC(f,x) = \frac{S(f,x)}{f \cdot E(f,x+2d)} \quad (9)$$

Where $S(f,x)$ corresponds to the discrete Fourier transform of the scattered field at a frequency *f* and an offset *x* and $E(f,x+2d)$ represents the discrete Fourier transform of the data from the model with no heterogeneities at the mirror position in respect of the crack of *x*.

To compute the dimensionless parameter to be studied, the wavelength (λ) corresponding to the frequency (*f*) analysed, can be retrieved by the expression: $\lambda = v/f$, where *v* corresponds to the surface wave medium velocity.

Fig. 24 illustrates the outcomes obtained using a 16 Hz Ricker pulse across a spectrum of cases featuring different crack sizes depths, ranging from 1 to 80 meters. These cases were examined at an offset of 200 meters from the crack position, maintaining a frequency of 16 Hz. As it can be seen, the value of the back-scattering coefficient rises for smaller cracks until it reaches a plateau when the crack size approximates one and a half times the wavelength utilised. This process can be explained by the concentration of surface wave energy typically within a depth equivalent to the wavelength of the wave. Consequently, as the crack size enlarges, it is reached a moment when the energy penetrating at greater depths becomes negligible, resulting to a stabilization of the energy back-scattered. The behaviour shown at

this plot, being normalised, should theoretically be extrapolated to any crack size and frequency.

Before verifying this last assertion, another feature present on the plot has to be commented. This feature is the presence of a region, that in this case ranges values of the dimensionless parameter between 0.1 to 0.3, where the back-scattering coefficient decreases, this effect is created due to a numerical error induced during the wave propagation simulation. This error induces a destructive interference that, for the smaller crack sizes models, reduces the amplitude values of certain frequencies.

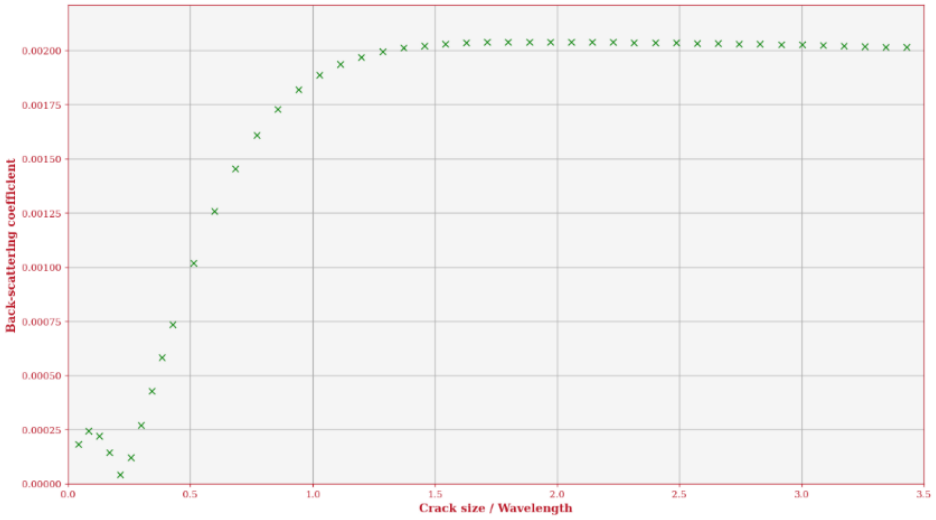

Figure 24: Results of the back-scattered coefficient obtained at an offset of 200 meters of the crack location at a frequency of 16 Hz by the use of a 16 Hz Ricker pulse plotted over the dimensionless parameter relating the crack size of the model computed and the wavelength of the frequency analysed.

To study if the behaviour of the back-scattering coefficient can be extrapolated, two approaches have been explored. Firstly, by obtaining the back-scattered coefficients for various frequencies ranging from 8 to 30 Hz in an offset of 200 meters, using as a source 16 Hz Ricker pulse. As it can be seen in Fig. 25, all the curves have collapsed to the same trend as an effect of the corrections. Comparing this behaviour and the one described in the previous plot it can be seen that they are the same, meaning that the normalised plot can be extrapolated to any frequencies. Only little discrepancies can be appreciated, probably due to numerical errors produced in the forward modelling.

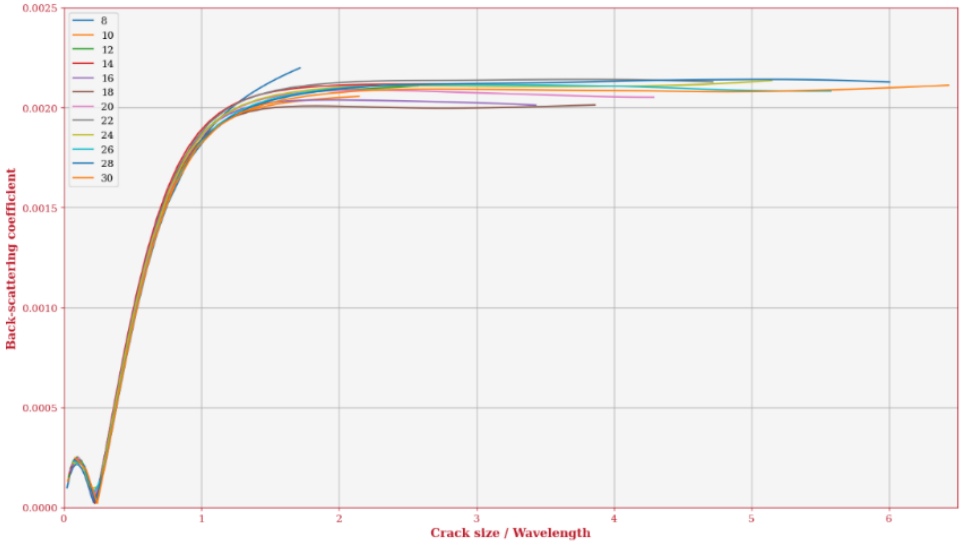

Figure 25: Results of the back-scattered coefficient at an offset of 200 meters of the crack location at a range of frequencies between 8 and 30 Hz obtained by the use of a 16 Hz Ricker pulse plotted over the dimensionless parameter relating the crack size of the model computed and the wavelength of the Ricker pulse used.

Finally, to further validate the extrapolation, a second method involves computing the back-scattering coefficient across a broad spectrum of frequencies and crack sizes. Fig. 26 provides a plot over the results shown in Fig. 24 (green crosses) whit the results obtained using a Ricker pulse of 20 Hz over crack sizes between 46 and 54 meters (black stars), the results obtained a Ricker pulse of 13 Hz over cracks with depths ranging between 60 and 66 meters (blue diamonds) and the results obtained over a crack of 50 meters of pulses having wavelengths linearly spaced between 18.65 and 37.30 meters (red circles). These results reaffirm the fact that the behaviour of the coefficient against the dimensionless parameter can be extrapolated for any frequency and crack size.

3.1.2 Layered case

To obtain the results for the layered case the procedure used is the same as for the homogeneous case, and as the relationship between frequency and velocity is constant for the range of frequencies studied, Eq. 9 can be used. For the layered case models have been generated for cracks ranging between 2 and 80 metres in intervals of 2 meters between models, which is the same region of study as the homogeneous case but with less models generated in the lower cracks range, which will imply a lower resolution in this range.

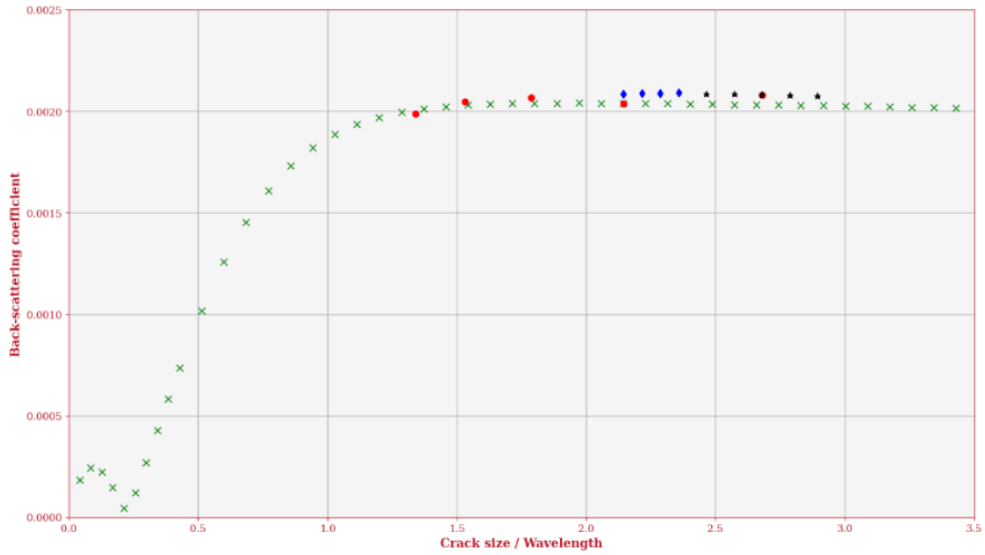

Figure 26: Results of the back-scattered coefficient at an offset of 200 meters of the crack location at a range of different frequencies and crack sizes obtained by the use of a Ricker pulse having at each time, the same frequency than the one analysed, plotted over the dimensionless parameter relating the crack size of the model computed and the wavelength of the Ricker pulse used.

Fig. 27 shows the results obtained for the back-scattering coefficient at an offset of 200 meters from the crack. The frequency studied is 16 Hz, which corresponds to the same frequency defined for the Ricker pulse to generate the data. As it can be seen, the behaviour obtained is the same as in the homogeneous case, where after a steep increase for the smaller cracks, a plateau is reached when the crack size is one a half times the wavelength corresponding to the frequency studied. In this case, the interference due to a numerical error is also present for the smaller cracks, but due to the lower resolution in this region, this error cannot be observed with the same shape as for the homogeneous study.

Once the behaviour of the layered cases has been observed to be consistent with the homogeneous, it is also studied if this behaviour can be extrapolated to any frequency and any crack. Same method as used in Fig. 25 is used, where back-scattering coefficients are obtained at different frequencies using a 16 Hz Ricker pulse as the source. Results, plotted in Fig. 28, show that the same behaviour is found for the different frequencies, although the precision of the results is lower than in the homogeneous case, as more numerical errors can be produced because of the presence of the different layers when producing the wavefield and also due to the lower information for smaller cracks. These results mean that the

assertion that back-scattering behaviour can be extrapolated can be extended to the layered case.

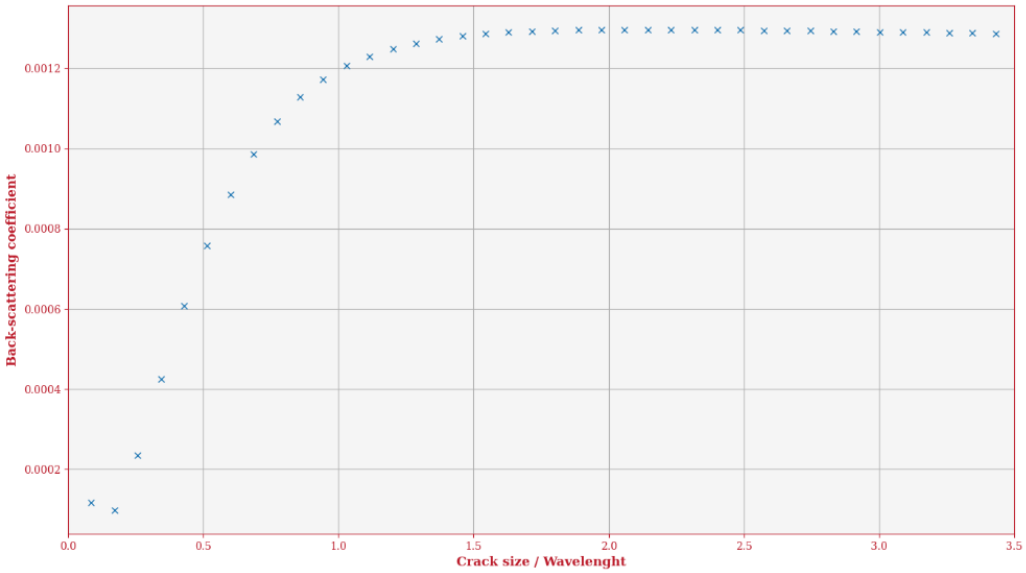

Figure 27: Results of the back-scattered coefficient obtained in a layered media at an offset of 200 meters of the crack location at a frequency of 16 Hz by the use of a 16 Hz Ricker pulse plotted over the dimensionless parameter relating the crack size of the model computed and the wavelength of the frequency analysed.

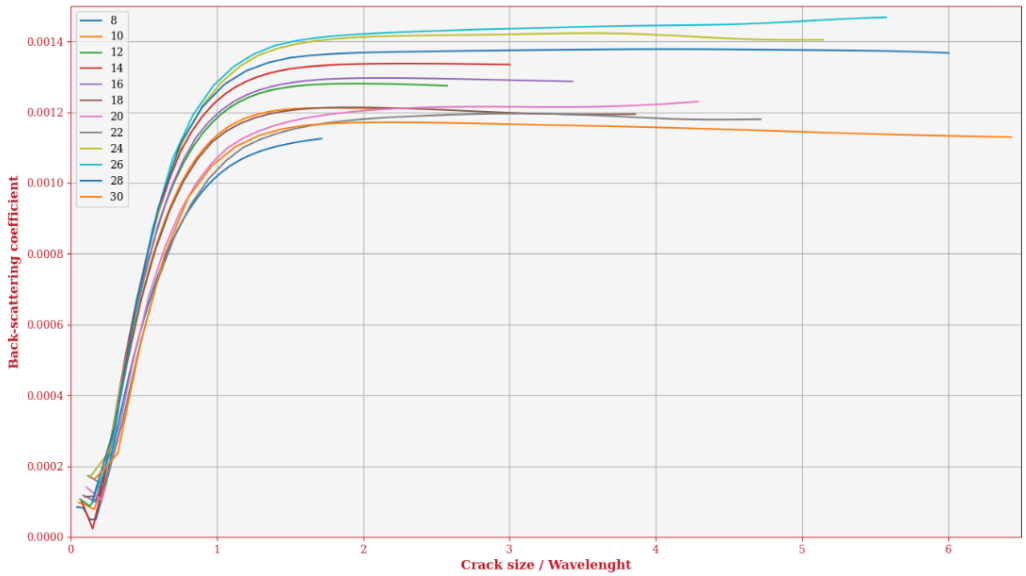

Figure 28: Results of the back-scattered coefficient in a layered media at an offset of 200 meters of the crack location at a range of frequencies between 8 and 30 Hz obtained by the use of a 16 Hz Ricker pulse plotted over the dimensionless parameter relating the crack size of the model computed and the wavelength of the Ricker pulse used.

3.2 3D directional response of a finite crack

Once the numerical study of the back-scattering produced by a crack is done for the 2D cases, the study of the 3D data is performed in a more analytical approach to understand how a heterogeneity can be located and migrated. To perform this study different approaches in various frameworks are applied to characterise different factors that affect the propagation of the scattering field.

3.2.1 2D sections of the 3D gather

The first framework approached is the study of different 2D sections of the 3D gather gathers produced over the 3D area to understand how the scattering produced by a 14-meter crack can be seen at different positions. Figs. 29-36 show 8 different 2D lines located at different distances to the shot and the scatterer. Each figure has four subplots, where different features are shown: on the upper left, the geometry of the 3D model, where the shot position and the 2D section studied are highlighted; on the upper right, the raw data obtained in the model without cracks; on the lower left, the synthetic gathers obtained by the 3D model with the presence of a crack; and on the lower right, the subtracted scattering field, which has a smaller amplitude scale, compared to the other shot gathers, which permits to observe clearly the different reflections and conversions.

Looking into the figures, it can be highlighted that the scattering field is easily detected as its amplitudes are in the same order of magnitude than the incident field, even higher for the larger offsets. The other main feature seen is that the position of the scatterer can be determined for the lines perpendicular to the crack, even if the study line does not cross it. This position corresponds to first value where reflections and conversions are detected in the scattering field. In the other cases, the scattering cannot be determined as the initial values detected are not located on the scattering positions. From which it can be determined that the position of the crack can only be directly determined if the study line crosses the scatter, or it is located strictly perpendicular to the heterogeneity.

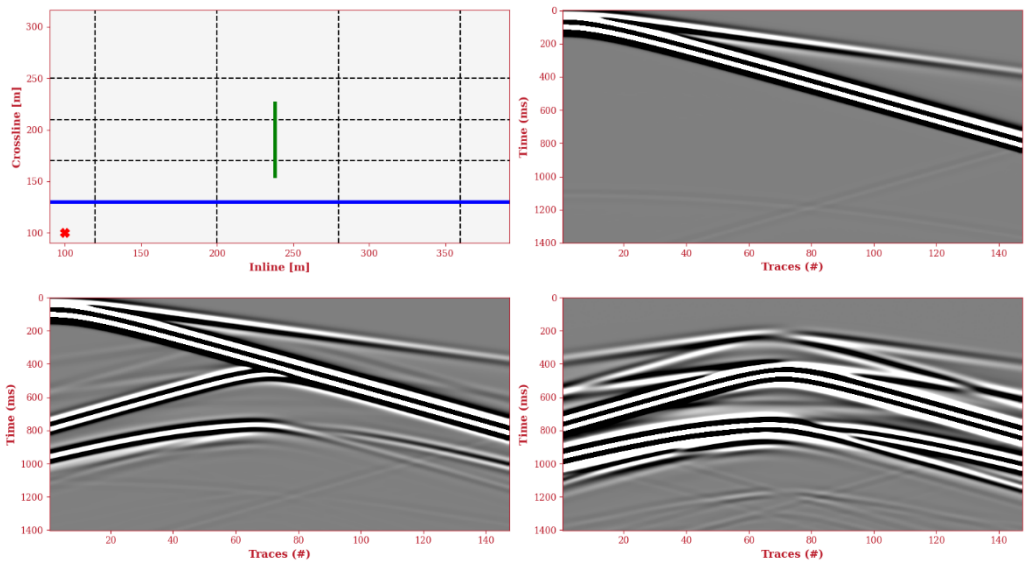

Figure 99: 130 meters crossline 2D section obtained from the 3D shot gather showing the geometry of the setup, the shot gather without crack, the shot gather with the crack and the scattering field obtained.

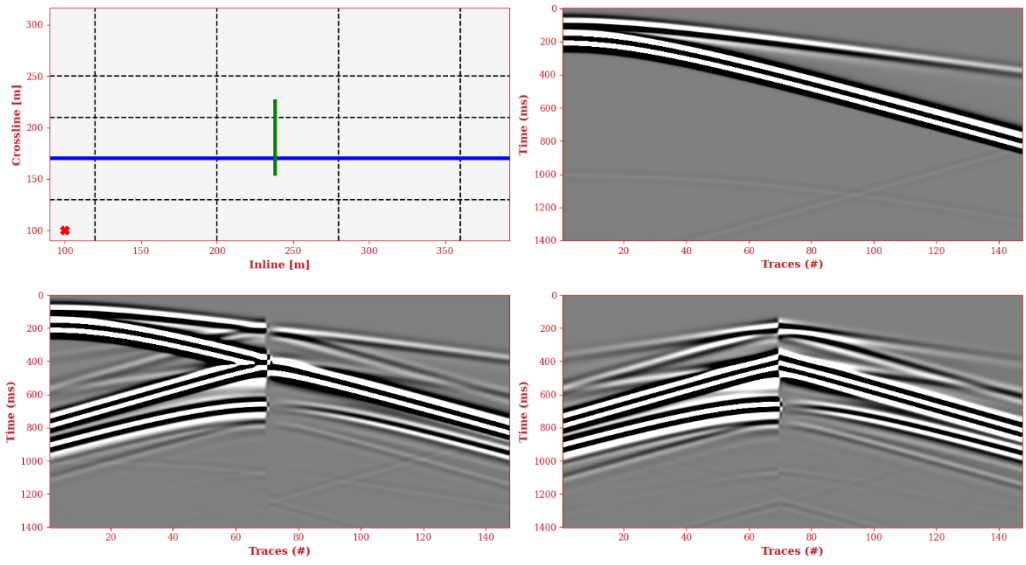

Figure 30: 170 meters crossline 2D section obtained from the 3D shot gather showing the geometry of the setup, the shot gather without crack, the shot gather with the crack and the scattering field obtained.

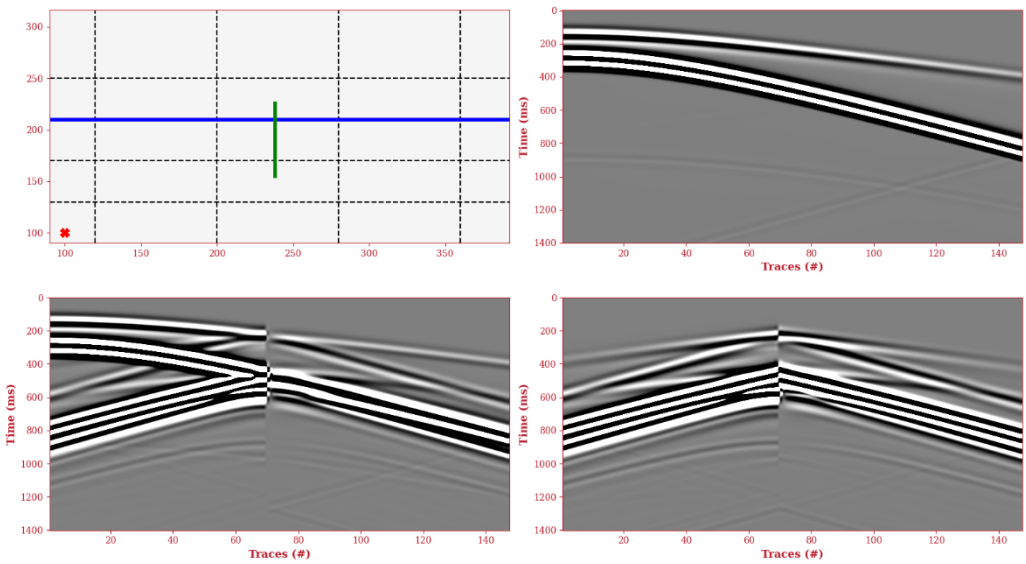

Figure 31: 210 meters crossline 2D section obtained from the 3D shot gather showing the geometry of the setup, the shot gather without crack, the shot gather with the crack and the scattering field obtained.

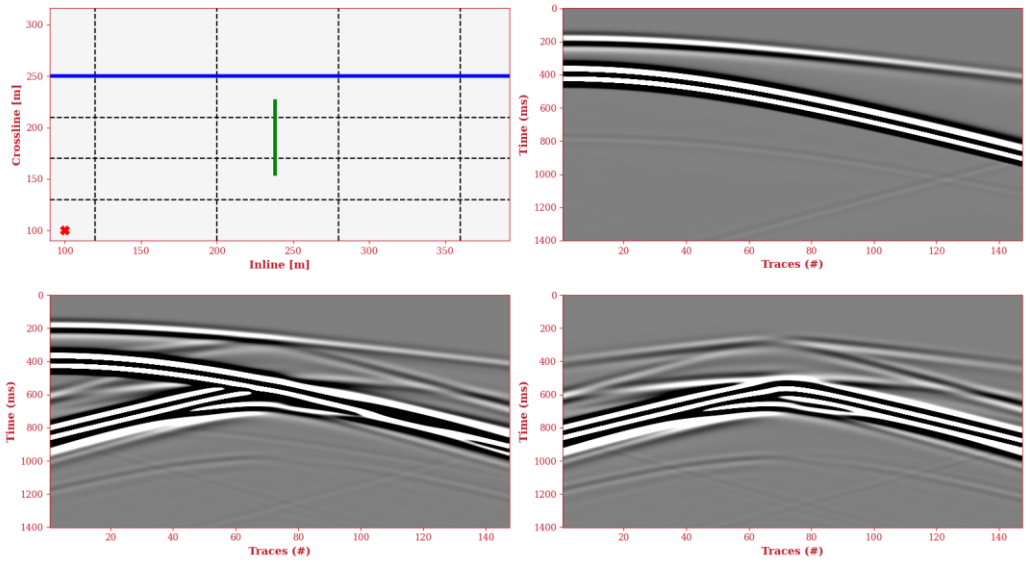

Figure 32: 250 meters crossline 2D section obtained from the 3D shot gather showing the geometry of the setup, the shot gather without crack, the shot gather with the crack and the scattering field obtained.

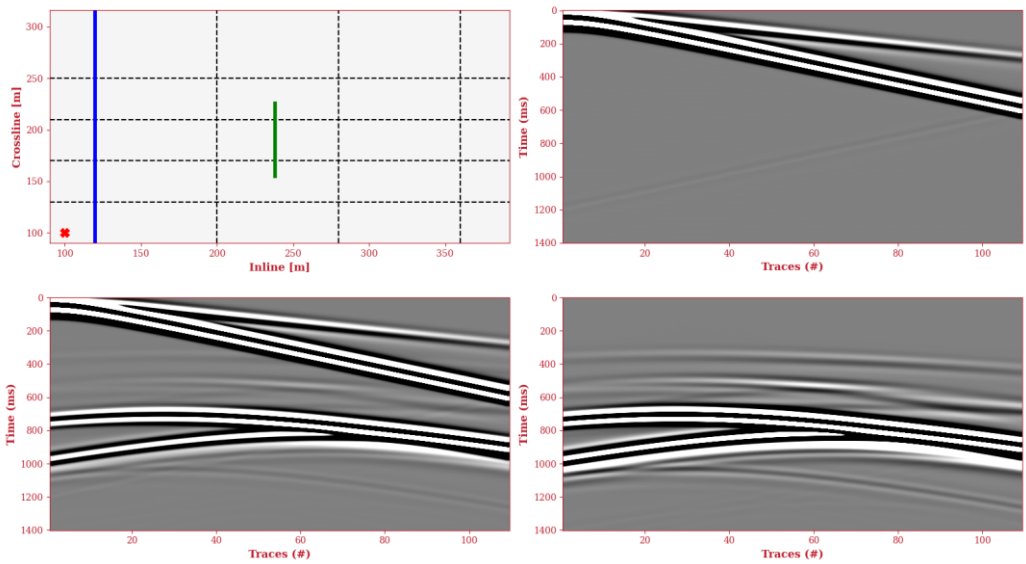

Figure 33: 120 meters inline 2D section obtained from the 3D shot gather showing the geometry of the setup, the shot gather without crack, the shot gather with the crack and the scattering field obtained.

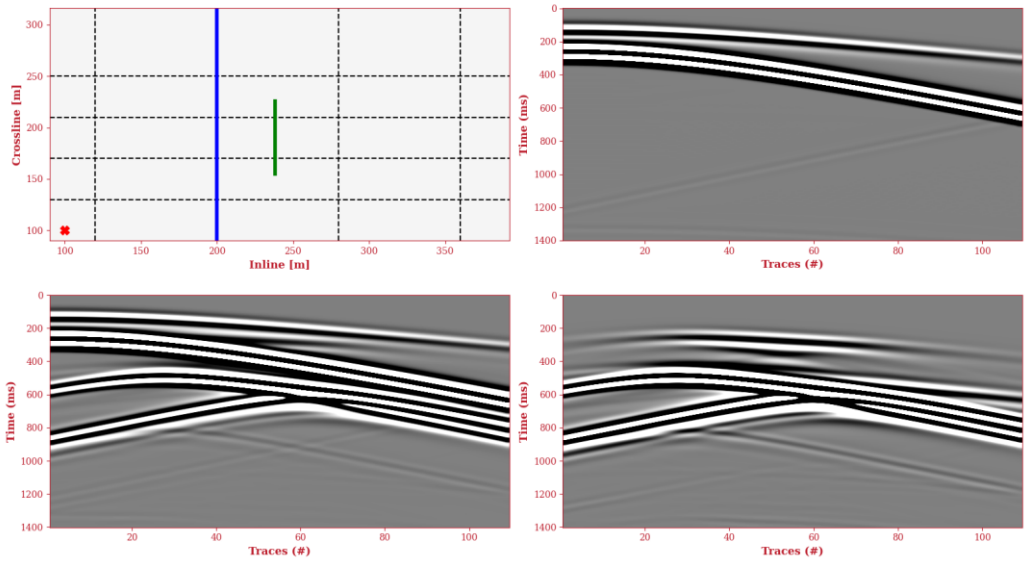

Figure 34: 200 meters inline 2D section obtained from the 3D shot gather showing the geometry of the setup, the shot gather without crack, the shot gather with the crack and the scattering field obtained.

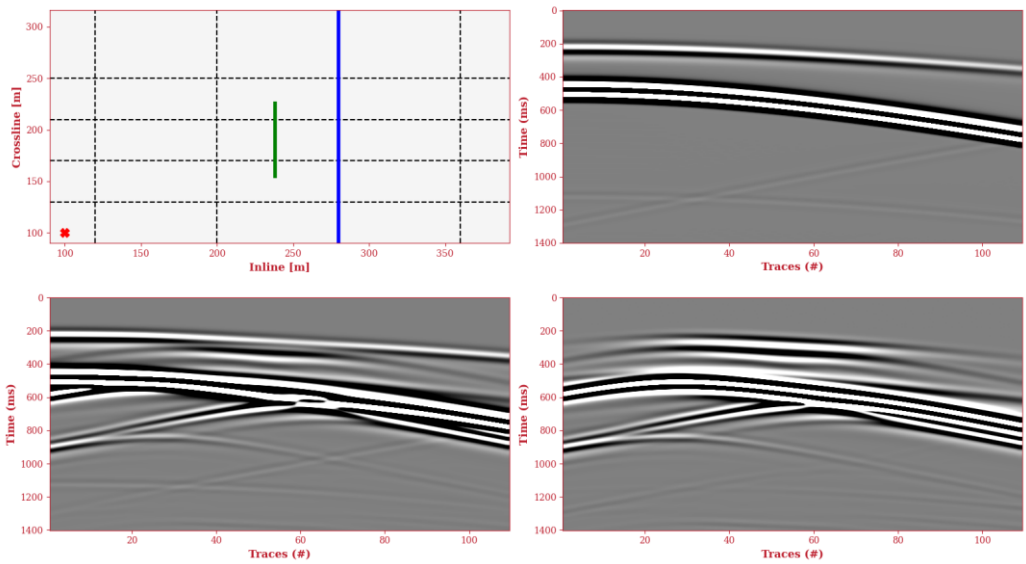

Figure 35: 280 meters inline 2D section obtained from the 3D shot gather showing the geometry of the setup, the shot gather without crack, the shot gather with the crack and the scattering field obtained.

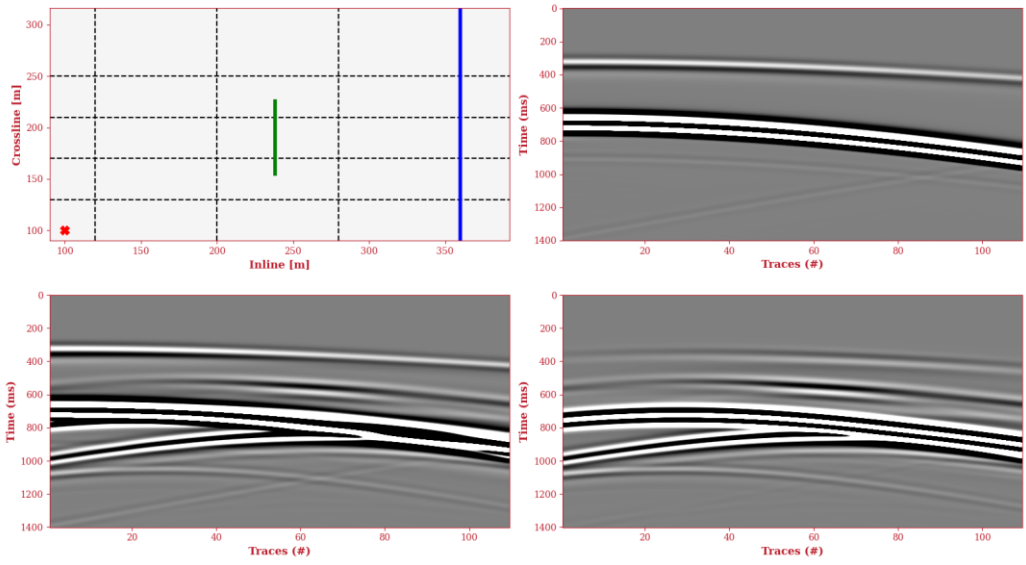

Figure 36: 360 meters inline 2D section obtained from the 3D shot gather showing the geometry of the setup, the shot gather without crack, the shot gather with the crack and the scattering field obtained.

3.2.2 Time slices

Another framework used to analyse the scattering field, is the study of the wave distribution in time over the whole surface of the 3D model. Fig. 37 shows some time slices obtained for the 60-meter crack for the times where the wavefront travels near the scatter, while Fig. 38 shows the same data for the crack of 14 meters depth. From these two plots, the diffractions produced at the borders of the crack can be seen from which it can be affirmed that their generation, shape and position is just a function of the geometry of the crack and of the shot position, as no major differences can be seen between the two models.

The only difference observable between the two models is the presence of some additional data on the forward-scattering zone for the 14-meter crack, highlighted in green at the 260 milliseconds time slice. This data corresponds to the scattering produced at the bottom of the crack which in the case of the 60-meter crack cannot be seen. This is because at that depth almost no energy is found, as energy is principally enclosed in depths smaller than the source wavelength (Section 3.3) which, for a 12 Hz source, it is 31.08 meters.

Focusing on the time slices for the 14-meter crack, comparing the amplitudes corresponding to the scattering field produced by the bottom of the crack and the amplitudes obtained by the scattering field produced by the reflections and diffractions, it can clearly be seen that the seconds are bigger. With this observation it can be stated that the scattering field is mostly influenced by lateral reflections and refractions and the scattering produced at the bottom can be neglected, especially for deeper cracks.

Another observation done by looking into the data for the 60-meter crack is that the crack produces a distortion of the incident wavefront, which produces a time delay to the part of the incident wave that interacts with the scatter.

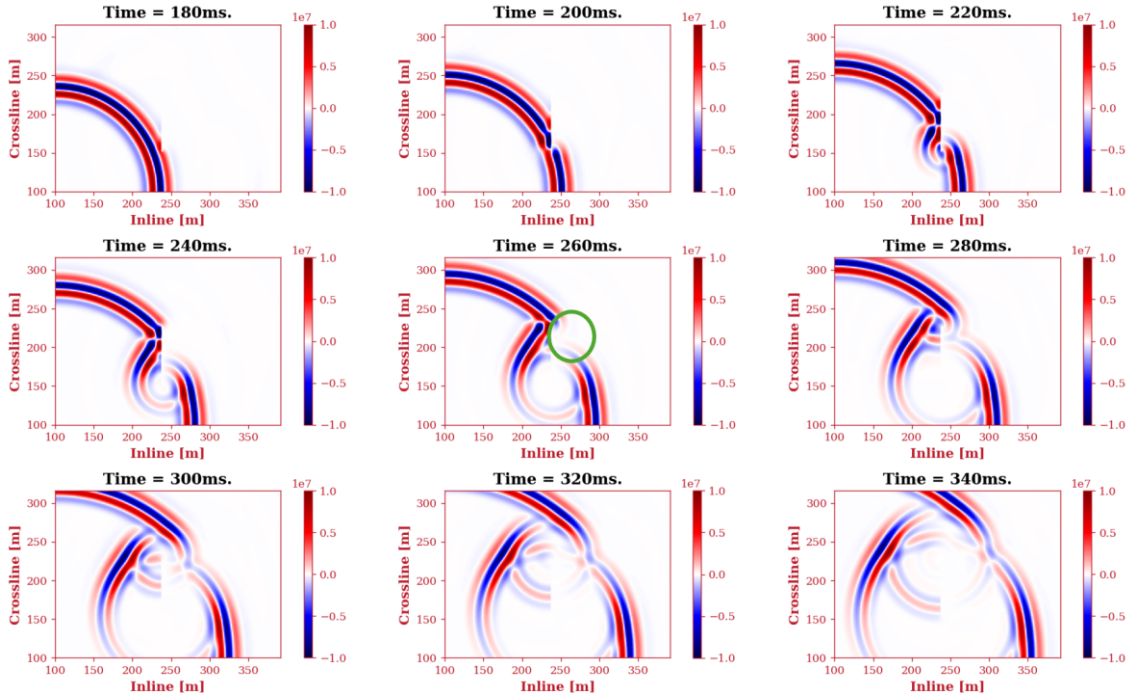

Figure 37: Time slices plots of the wavefield amplitudes distribution at the surface for a 3D model with the presence of a 60-meter crack.

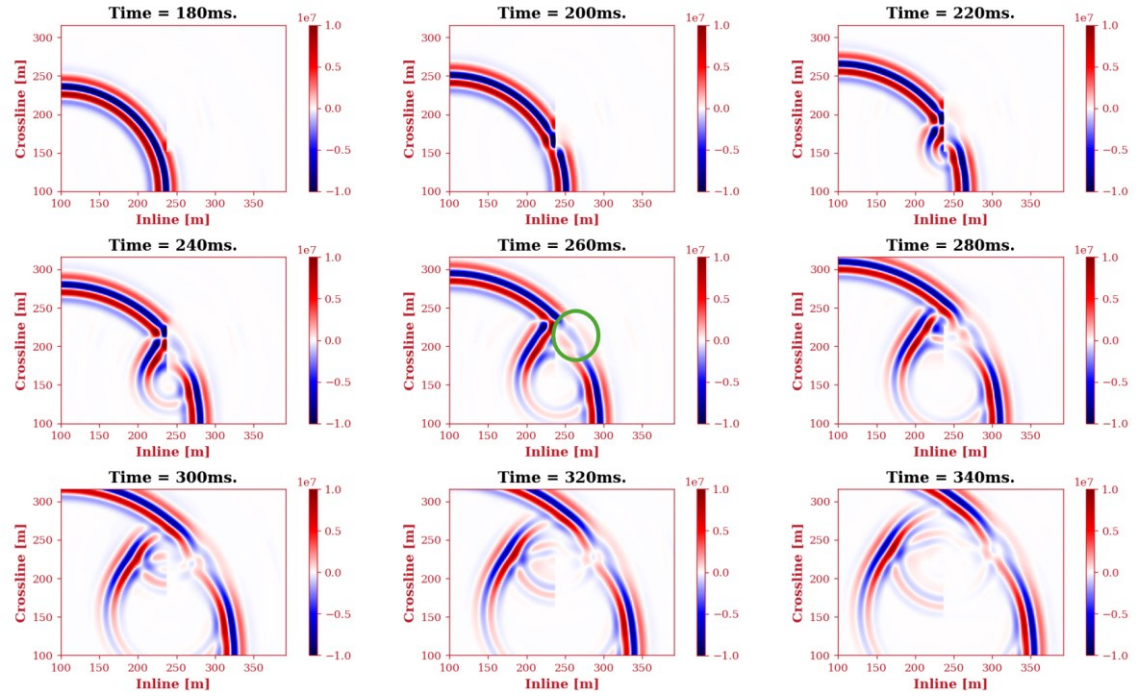

Figure 38: Time slices plots of the wavefield amplitudes distribution at the surface for a 3D model with the presence of a 14-meter crack.

3.2.3 Directivity

As noted in Section 3.2.1, the position of the scatter cannot be directly obtained from looking at the shot gathers unless the line crosses the heterogeneity or is locater perpendicular to the crack. For that reason, to locate the heterogeneity location and also to understand how the migration can be done, an amplitude distribution study of the scattering field can be performed.

Figs. 39-43 show the plots obtained for the scattering field where the maximum amplitude in time domain recorded at each receiver is shown for all the shots located at an inline of 100 meters. On them it can be observed that the shape of this plots is almost symmetrical in both sides of the crack. By drawing on the figures the lines corresponding to the reflections produced at the borders of the crack, it can be recognised that the bigger values are found in the area between both lines.

From these observations, it can be concluded that the energy produced by the scattering is focused into a direction which corresponds to the area where rays are reflected by the heterogeneity. In this area, reflections create a constructive interference with diffractions, which are present over the hole model that make the amplitude values to rise.

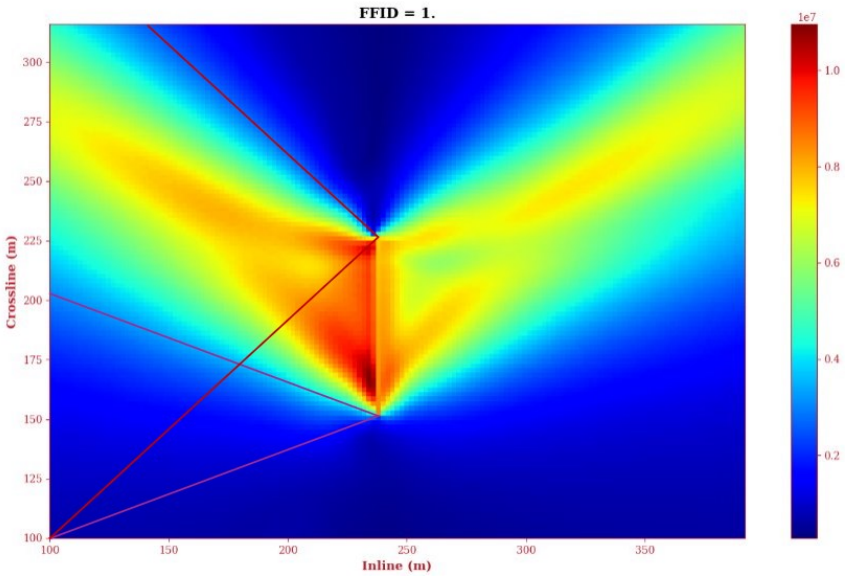

Figure 39: Scattering field maximum amplitudes in time domain at each receiver obtained by a shot located at the coordinate (100,100). Lines correspond to the reflection path at both extremes of the crack.

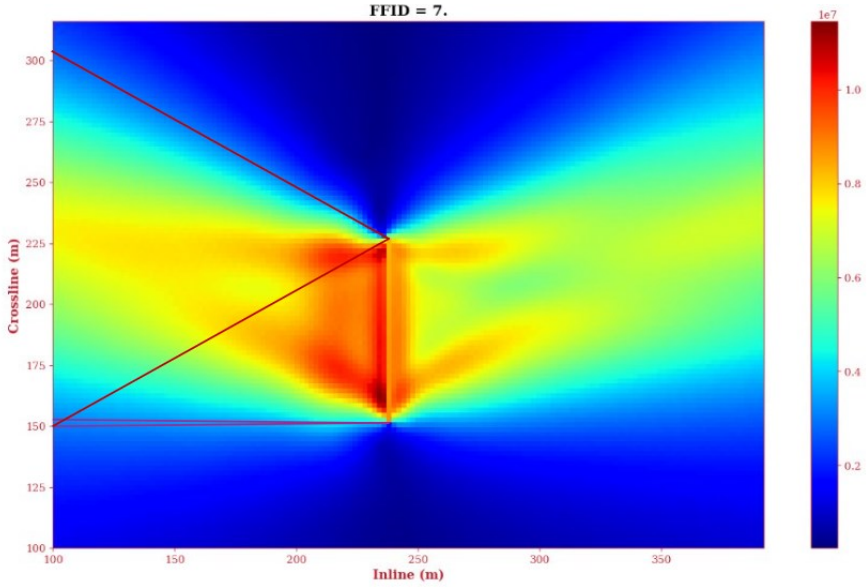

Figure 40: Scattering field maximum amplitudes in time domain at each receiver obtained by a shot located at the coordinate (100,150). Lines correspond to the reflection path at both extremes of the crack.

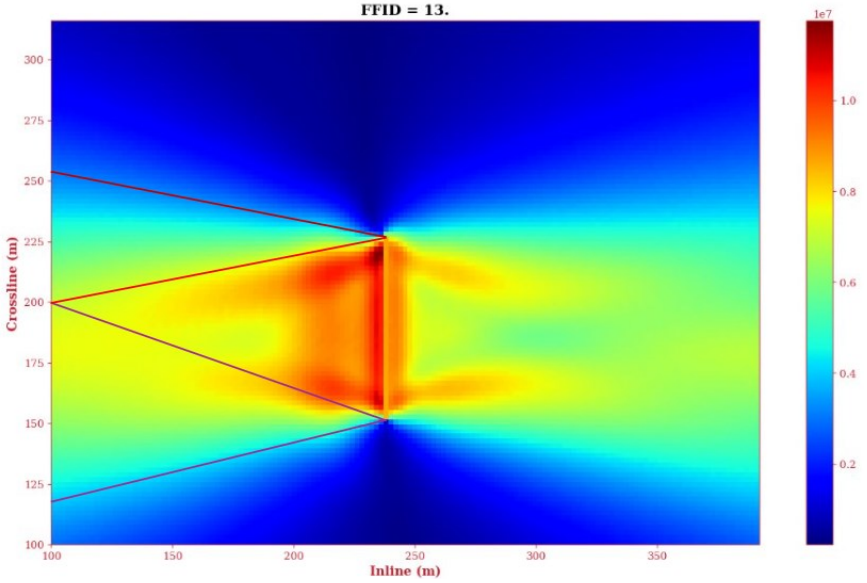

Figure 41: Scattering field maximum amplitudes in time domain at each receiver obtained by a shot located at the coordinate (100,200). Lines correspond to the reflection path at both extremes of the crack.

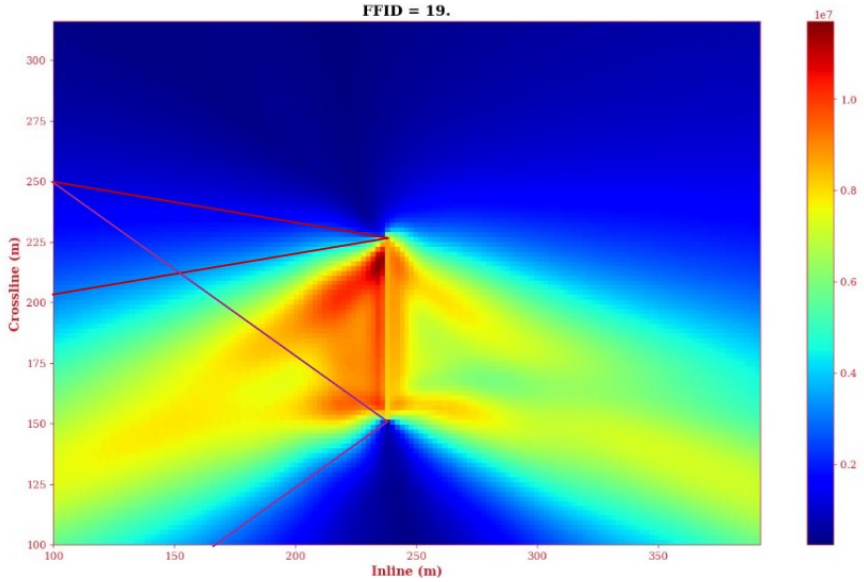

Figure 42: Scattering field maximum amplitudes in time domain at each receiver obtained by a shot located at the coordinate (100,250). Lines correspond to the reflection path at both extremes of the crack.

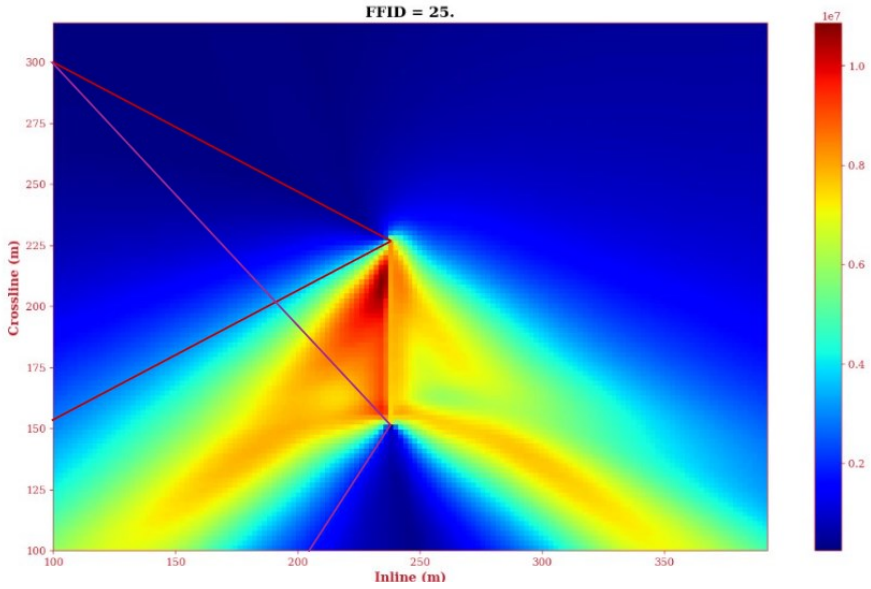

Figure 43: Scattering field maximum amplitudes in time domain at each receiver obtained by a shot located at the coordinate (100,300). Lines correspond to the reflection path at both extremes of the crack.

3.2.4 2D amplitude slices

Once the maximum amplitudes in space are displayed, they can also be displayed on some lines parallel to the scatterer, in order to see if it is possible from the maximum amplitudes to obtain some numerical information about the scatter location.

Fig. 44 shows the amplitudes obtained for the shot located at coordinates (100, 200) at all receivers located at the same inline value, where a peak is observed at a crossline position of approximately 180 meters. In this case, this point is at a crossline distance of 20 meters from the shot position. Which means that the position where the wave has been reflected corresponds to half distance between these two points, which corresponds to 190 meters. Remaining that the crack in the crossline direction is extended from 153.25 to 227.5 meters it can be see seen that the centre of the crack is located at 190.375 meters.

Doing the same procedure for the shot at coordinates (100, 100), the amplitude peak is located around 288 meters (Fig. 45), which corresponds to a reflection point located around 189 meters. From these results and considering possible numerical errors, it can be stated that the central position of the scatter can be obtained considering that the amplitude peak value corresponds to the reflection from this point.

Lastly, Fig. 46 shows the amplitudes corresponding to all receivers located at the same inline than the shot located at coordinates (150, 200). On this case two peaks are found: this is because the distance from the scatter is not long enough to permit these picks to focus on the position corresponding to the reflexion of the centre of the scatter. This behaviour can be observed for offsets near the scatterer in the maximum amplitude distribution plots shown in the previous section. In these cases, is not possible to obtain the position of the scatter centre, instead by studying the reflection points at the two peaks, information of the minimum dimensions of the scatterer can be obtained.

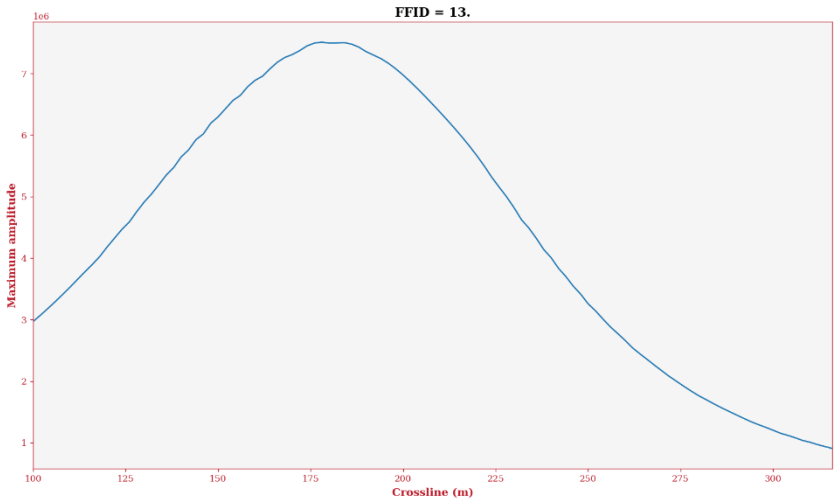

Figure 44: Plot of the scattering field maximum amplitude registered at each receiver at an inline position equal to 100 meters by a shot located at the coordinate (100, 200).

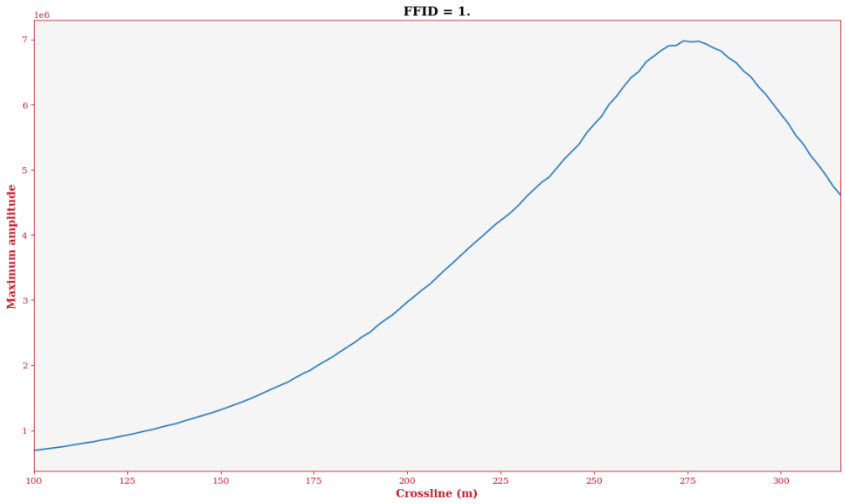

Figure 45: Plot of the scattering field maximum amplitude registered at each receiver at an inline position equal to 100 meters by a shot located at the coordinate (100, 100).

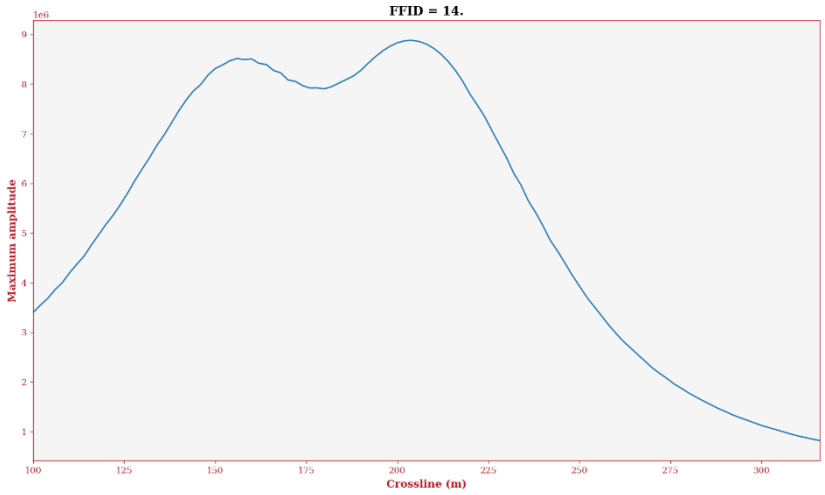

Figure 46: Plot of the scattering field maximum amplitude registered at each receiver at an inline position equal to 150 meters by a shot located at the coordinate (150, 200).

3.2.5 Geometrical analysis

Following, a geometrical analysis is performed in order to study the effects of the geometry on the results obtained. As the scatterer is not located symmetrically to the shot positions, some differences in distance are found between shots on the left of the heterogeneity and on the right.

For this study, shots at locations at (100, 100) and (100, 350) are considered. These two shots are almost in mirror position with respect to the crack, where there is just a difference in distance of 26 meters in the inline direction between the shots and the crack. Starting the study with 2D sections of the 3D gather for the same crossline values (Fig. 47), as it can be seen while the crack produces a phase inversion in the back-scattering field for the first shot, in the case of the second shot this phase inversion is not found.

Same thing is obtained by plotting the same scattering field time slice (Fig. 48), although the non-zero amplitudes are not located at the same locations as for the second shot the travel time is smaller, in can be observed the phase change for the first shot which does not occur for the second.

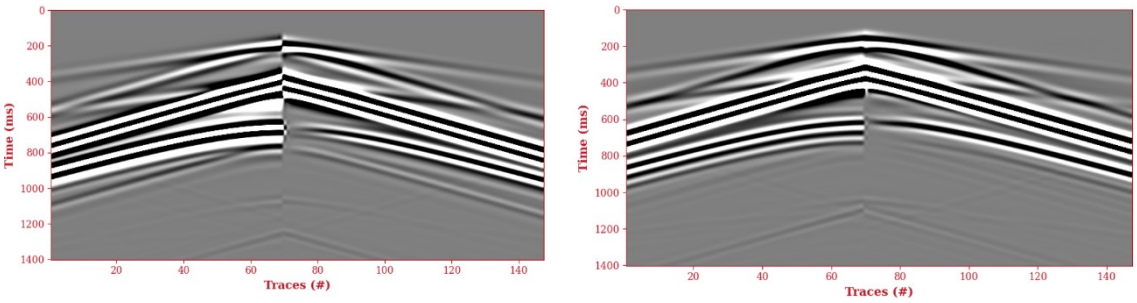

Figure 47: 170 meters crossline 2D section comparison between a shot located at coordinates (100,100), on the left, and a shot located at (100, 350), on the right.

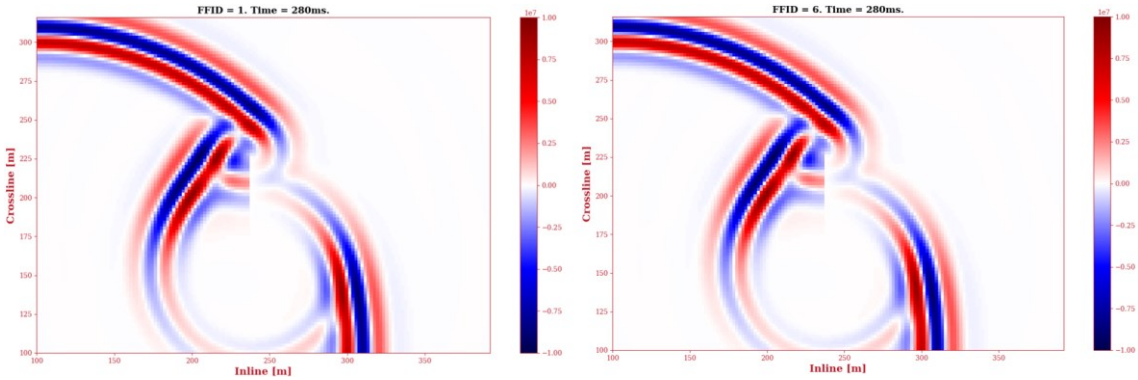

Figure 48: Time slices amplitude wavefield comparison at 240 ms between a shot located at coordinates (100,100), on the left, and a shot located at (100, 350), on the right.

Lately, a comparison of the maximum amplitudes of the scattering field is performed. If the geometry does not affect, same values should be fined in the mirror positions to the scatter between both shots. As it can be seen in Fig. 49, this do not happen. What it can be seen is

that for the first shot the maximum values are located in the back-scattering side. Meanwhile, for the second shot, amplitudes are bigger in the forward-scattering side.

From this geometrical study, it can be stated that the geometry also takes a part on the scattering energy distribution, as it affects the constructive and destructive interferences between reflections, diffractions and conversions.

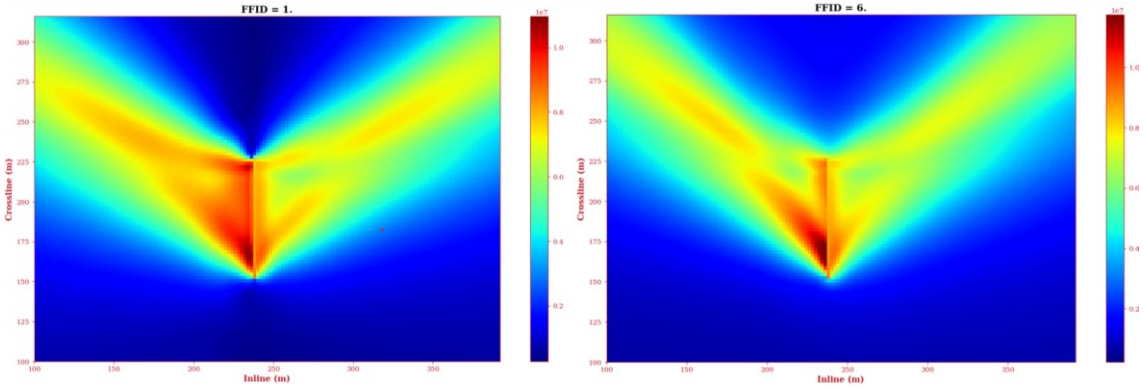

Figure 49: Scattering field maximum amplitudes comparison between a shot located at coordinates (100,100), on the left, and a shot located at (100, 350), on the right.

3.3 Energy distribution with depth

Using the procedure explained at Section 2.4.1, energy distribution with depth plots can be obtained from the vertical component of surface waves amplitude distribution with depth. Fig. 50 presents the results derived from the amplitudes of a 16 Hz surface wave on a homogeneous half-space (Fig. 22). To provide meaningful results, the behaviour has been normalised into the percentage of cumulative energy, revealing that nearly all the energy is concentred within a depth corresponding to the first wavelength ($\lambda \approx 23.3$ m), as expected from the amplitudes distribution with depth.

Following the same procedure presented in the Methods section, the results for a 16 Hz surface wave are compared with the 6 Hz case. Fig. 51 presents the results obtained for a surface wave of 6 Hz in a homogeneous half-space, whose amplitudes are shown in Fig. 23. Although the dimension of the depth axis changes compared to Fig. 50, as also seen in the previous chapter for the amplitude distribution with depth, the results are consistent as in

both cases the shape is the same and energy values tend to be 100% for depths corresponding to one wavelength ($\lambda \approx 62.16$ m for 6 Hz).

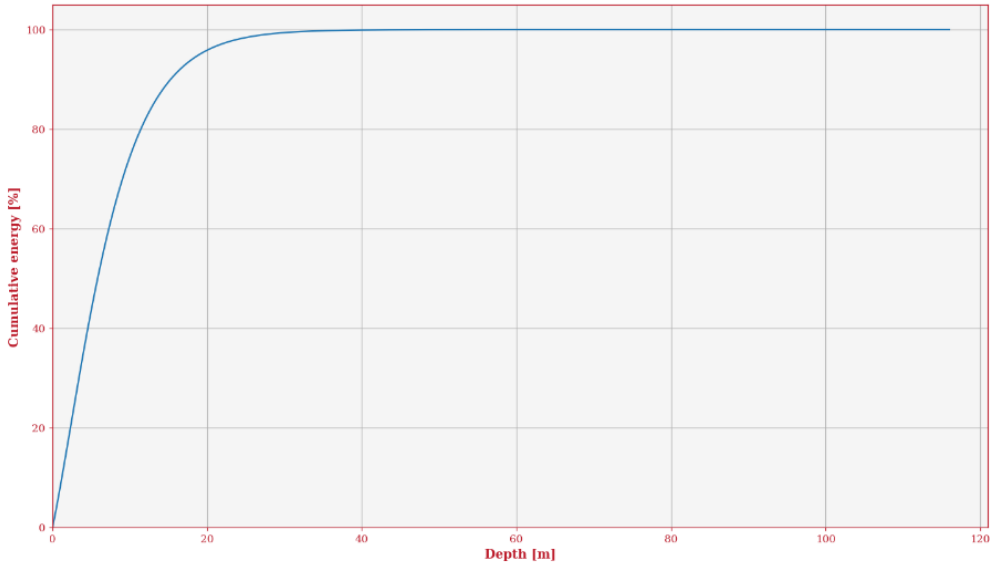

Figure 50: Plot of the cumulative energy percentage of a 16 Hz surface wave in a homogeneous half-space as a function of depth.

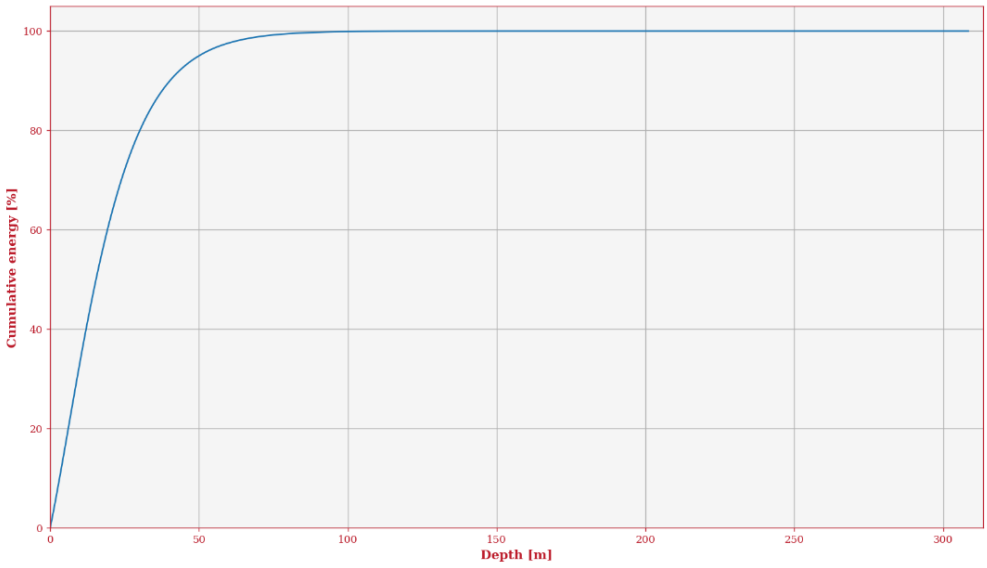

Figure 51: Plot of the cumulative energy percentage of a 6 Hz surface wave in a homogeneous half-space as a function of depth.

4. Discussion

In this chapter the discussion of the results introduced in the previous chapter is presented. Initially, the results obtained from 2D homogeneous half-space models are evaluated, which show a consistent relationship between the cumulative energy and back-scattering coefficient results, whose consequences are evaluated. Next, using the characteristics identified from the results of the 3D models, the ideas of the possibility to locate and migrate heterogeneities in real seismic surveys are discussed.

As just indicated, by comparing the behaviour of the normalised cumulative energy and the normalised back-scattering coefficient at identical frequencies it can be seen that both properties exhibit the same behaviour, as illustrated in Fig. 52. The back-scattering coefficient values have been slightly shifted in order to corroborate the that the relation is consistent without the values heavily affected by the numerical error induced. As shown, both lines are nearly in perfect alignment, with only minor differences influenced by numerical errors and the applied shift.

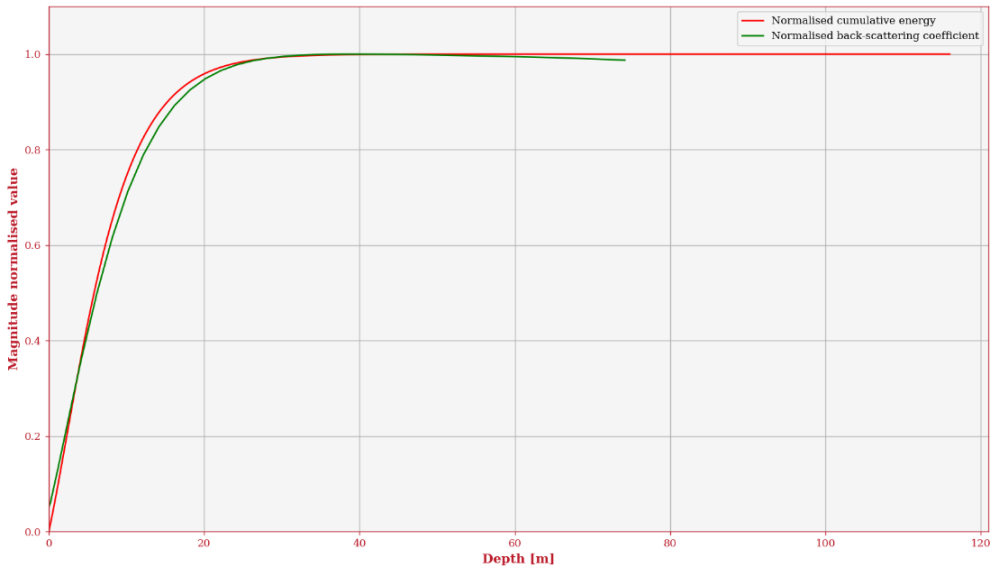

Figure 52: Normalised plot against depth to compare the values of the cumulative energy and the back-scattering coefficient.

This correlation offers the possibility to predict the back-scattering coefficient for any crack at a given frequency. The only requirements are the vertical component of the surface wave

eigenfunction and a single back-scattering value corresponding to a specific crack size at the same frequency. Since computing the surface wave eigenfunction is significantly faster than obtaining back-scattering coefficient values for different crack sizes or frequencies, this relationship permits the saving of time and computational resources.

Focusing into the results obtained for a 3D homogeneous model it can be stated that the observed waveform of the back-scattered (reflected and diffracted) surface wave field shows that the secondary wavefield can be represented using the Huygens' principles as the superposition of secondary point sources, as summarised in Fig. 53.

After analysing the directivity results obtained for the secondary (scattering) field, it can be stated that it is clearly related to the geometry of the scatterer: this implies that the analysis of the scattering can reveal the shape and position of the scatterer.

The shape of the scattered wavefield confirms that the 3D migration of the scattering can collapse the energy on the scatterer: this will image the scatterer itself but also provide a model of the scattering for its attenuation when it is considered as noise in active seismic data.

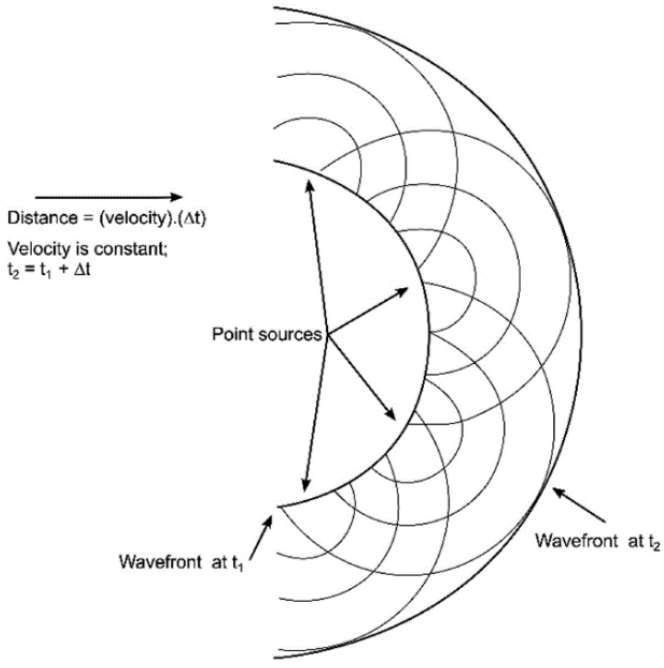

Figure 53: Huygens' principle schematic image where is shown how a wavefield can be represented as a superposition of point sources. Figure from Tylor-Jones et al. (2022)

5. Conclusion and future work

In this master thesis a study of the scattering produced by surface cracks in different models has been presented in order to understand this type of heterogeneities, which can become a potential hazard in subsurface exploitation activities.

The use of several 2D synthetic models with the presence of surface cracks of different sizes has revealed that the magnitude of the scattering field produced increases with the dimension of the crack, until reaching a plateau for depths bigger than the wavelength of the studied frequency. This behaviour has been studied numerically by the definition of the back-scattering coefficient, which has proved to be equal for any frequency over a dimensionless domain.

Also, it has been demonstrated that, for the same frequency, the normalised values of the back-scattering coefficient against the crack depth are the same as the ones obtained for the normalised cumulative energy of a surface wave with depth. This relationship permits the prediction of the back-scattering coefficient for any crack size and frequency, permitting the saving of time and computational resources. It is only needed the value of the back-scattering coefficient for a certain crack and frequency and the amplitudes eigenfunction of the surface wave in depth at the studying frequency.

The study of the back-scattering coefficient can be extended in future works to other near-surface heterogeneities such as sub-surface cracks, steps or cavities of different shapes. Where the results obtained, can be analysed against dimensionless magnitudes to study possible consistent behaviours for different frequencies or, in the case of sub-surface bodies, do a study against the size to depth ratio of the heterogeneities to investigate potential interesting behaviours.

Using the 3D models, the scattering field has been qualitatively analysed to characterise the feasibility to locate and migrate heterogeneities in real cases. From the study of 2D sections of the 3D shot gather, amplitudes distribution in time and maximum amplitudes it has been observed that the scattering field, mostly controlled by the lateral shape of the heterogeneity, is stronger in the reflection zone of the crack, focusing on the direction of the centre of the crack reflection. Moreover, it has been observed that the shot geometry also affects the scattering field as different interference patterns are found.

Finally, from the results observed for the 3D models it has been concluded that it is feasible to migrate the scattering field in real data as the scattering field can be represented using the Huygens' principle. Also, as the field directivity is related to the position and shape of the scatterer, this can be located and characterised.

References

Achenbach, J.D., Gautesen, A.K. & Mendelsohn, D.A. (1980). Ray Analysis of Surface-Wave Interaction with an Edge Crack. *IEEE Transactions on Sonics and Ultrasonics*, 27(III), 124-129. https://doi.org/10.1109/T-SU.180.31161

Achenbach, J.D. & Brind, R.J. (1981). Scattering of surface waves by a sub-surface crack. *Journal of Sound and Vibration*, 76(I), 43-56. https://doi.org/10.1016/0022-460X(81)90289-3

Bačić, M., Librić, L., Kaćunić, D.J. & Kovačević, M.S. (2020). The Usefulness of Seismic Surveys for Geotechnical Engineering in Karst: Some Practical Examples. *Geosciences*, 10(10), 406. https://doi.org/10.3390/geosciences10100406

Båth, M. (1979). *Introduction to Seismology* (1st ed.). Birkhäuser. https://doi.org/10.1007/978-3-0348-5283-8

Blake, R.J. & Bond, L.J. (1990). Rayleigh wave scattering from surface features: wedges and down-steps. *Ultrasonics*, 28(4), 214-228. https://doi.org/10.1016/0041-624X(90)90089-7

Bohren, C.F. & Huffman, D.R. (1998). *Absorption and Scattering of Light by Small Particles* (1st ed.). Wiley. https://doi.org/10.1002/9783527618156

Bormann, P., Engdahl, B., Kind, R. (2012). Seismic Wave Propagation and Earth models. In Bormann, P. (Ed.), *New Manual of Seismological Observatory Practice 2 (NMSOP2)* (1st ed., pp. 1-105). Deutsches GeoForschungsZentrum GFZ. https://doi.org/10.2312/GFZ.NMSOP-2_ch2

Budaev, B.V. & Bogy, D.B. (1995). Rayleigh wave scattering by a wedge. *Wave motion*, 22(3), 239-257. https://doi.org/10.1016/0165-2125(95)00023-C

Budaev, B.V. & Bogy, D.B. (1996). Rayleigh wave scattering by a wedge II. *Wave motion*, 24(3), 307-314. https://doi.org/10.1016/S0165-2125(96)00024-8

Burger, H. R., Sheehan, A. F., & Jones, C. H. (2006). *Introduction to Applied Geophysics: Exploring the Shallow Subsurface* (1st ed.). Cambridge University Press. https://doi.org/10.1017/9781009433112

Chai, H., Phoon, K., Goh., S & Wei, C. (2012). Some theoretical and numerical observations on scattering of Rayleigh waves in media containing shallow rectangular cavities. *Journal of Applied Geophysics*, 83, 107-119. https://doi.org/10.1016/j.jappgeo.2012.05.005

Chai, H., Goh, S., Phoon, K., Wei, C. & Zhang, D. (2014). Effects of source and cavity depths on wave fields in layered media. *Journal of Applied Geophysics*, 107, 163-170. https://doi.org/10.1016/j.jappgeo.2014.05.017

Cook, D.A. & Berthelot, Y.H. (2001). Detection of small surface-breaking fatigue cracks in steel using scattering of Rayleigh waves. *NDT & E International*, 34(7), 483-492. https://doi.org/10.1016/S0963-8695(00)00080-3

Díaz, J., Ruiz, M., Sánchez-Pastor, P.S. & Romero, P. (2017). Urban Seismology: on the origin of earth vibrations within a city. *Scientific Reports*, 7, 15296. https://doi.org/10.1038/s41598-017-15499-y

Feynman, R. P., Leighton, R. B., & Sands, M. (1963). The Feynman Lectures on Physics. Addison-Wesley.

Foti, S., Lai, C., Rix, G.J. & Strobbia, C. (2015). *Surface Wave Methods for Near-Surface Site Characterization* (1st ed.). CRC Press. https://doi.org/10.1201/b17268

Foti, S., Hollender, F., Garofalo, F. et al. (2018). Guidelines for the good practice of surface wave analysis: a product of the InterPACIFIC project. *Bulletin of Earthquake Engineering*, 16, 2367–2420. https://doi.org/10.1007/s10518-017-0206-7

Hess, P. (2002). Surface Acoustic Waves in Materials Science. *Physics Today*, 55(3), 42–47. https://doi.org/10.1063/1.1472393-

Ji, S., Sun, S., Wang, Q. & Marcotte, D. (2010). Lamé parameters of common rocks in the Earth's crust and upper mantle. *Journal of Geophysical Research*, 115, B06314. https://doi.org/10.1029/2009JB007134

Johansen, E.L. (1967). Surface wave scattering by a Step. *IEEE Transactions on Antennas and Propagation*, 15(III), 442-448. https://doi.org/10.1109/TAP.1967.1138920

Kearey, P., Brooks, M. & Hill, I. (2002). *An introduction to geophysical exploration* (3rd ed). Oxford: Blackwell Science.

Kennett, B.L.N. (2009). *Seismic Wave Propagation in Stratified* Media. ANU Press. http://www.jstor.org/stable/j.ctt24h2zr.4

Lavergne, M. (1989). *Seismic Methods* (1st ed.). Éditions Technip.

Laske, G. & Widmer-Schnidrig, R. (2015). 1.04 - Theory and Observations: Normal Mode and Surface Wave Observations. In Schubert, G. (Ed.), *Treatise on Geophysics* (2nd ed., pp. 117-167). Elsevier. https://doi.org/10.1016/B978-0-444-53802-4.00003-8

Likharev, K.K. (2022). Wave Scattering. In *Essential Graduate Physics – classical Electrodynamics.* Stony Brook University. Retrieved May 22, 2024, from https://phys.libretexts.org/@go/page/57026

Lines, L.R., Slawinski, R.R. & Bording, P. (1999). A recipe for stability of finite-difference wave-equation computations. *Geophysics,* 64 (3), 967–969. https://doi.org/10.1190/1.1444605

Liu, S., Sung, J. & Chang, C. (1996). Transient scattering of Rayleigh waves by surface-breaking and sub-surface cracks. *International Journal of Engineering Science*, 34(9), 1059-1075. https://doi.org/10.1016/0020-7225(95)00143-3

Love, A. E. H. (1911). *Some Problems of Geodynamics*. Cambridge University Press.

Margerin, L. (2011). Seismic Waves, Scattering. In Gupta, H.K. (Ed.), *Encyclopedia of Solid Earth Geophysics* (pp. 1210-1223). Springer. https://doi.org/10.1007/978-90-481-8702-7_54

Mendelsohn, D.A., Achenbach, J.D. & Keer, L.M. (1980). Scattering of elastic waves by a surface-breaking crack. *Wave motion,* 2, 277-292. https://doi.org/10.1016/0165-2125(80)90008-6

Mufti, I. R. (1990). Large-scale three-dimensional seismic models and their interpretive significance. *Geophysics*, 55(9), 1166–1182. https://doi.org/10.1190/1.1442933

Munasinghe, M. & Farnell, G.W. (1973). Rayleigh Wave Scattering in Layered Media. *1973 Ultrasonics Symposium*, 506-509. https://doi.org/10.1109/ULTSYM.1973.196253

Quarteroni, A. (2016). *Numerical Models for Differential Problems* (2nd ed.). Springer. https://doi.org/10.1007/978-88-470-5522-3

Rayleigh, L. (1885). On Waves Propagated along the Plane Surface of an Elastic Solid. *Proceedings of the London Mathematical Society*, 17, 4-11. https://doi.org/10.1112/plms/s1-17.1.4

Riyanti, C.D. & Herman, G.C. (2005). Three-dimensional elastic scattering by near-surface heterogeneities. *Geophysical Journal International*, 160(2), 609-620. https://doi.org/10.1111/j.1365-246X.2005.02492.x

Rodríguez-Castellanos, A., Ávila–Carrera, R. & Sánchez–Sesma, F. J. (2007). Scattering of Rayleigh-waves by surface-breaking cracks: an integral formulation. *Geofísica Internacional* 46(4), 241-248. http://www.scielo.org.mx/scielo.php?script=sci_arttext&pid=S0016-71692007000400003&lng=es&tlng=en

Schumaker, D. (2006). *Earthquake Seismogram* [Image]. Flickr. https://www.flickr.com/photos/rockbandit/309794495.

Sengbush, R.L. (1983). *Seismic Exploration Methods*. Springer. https://doi.org/10.1007/978-94-011-6397-2

Shapiro, S.A. & Kneib, G. (1993). Seismic Attenuation By Scattering: Theory and Numerical Results. *Geophysical Journal International*, 114(2), 373–391. https://doi.org/10.1111/j.1365-246X.1993.tb03925.x

Shearer, P.M. (2009). *Introduction to Seismology* (2nd ed.). Cambridge University Press. https://doi.org/10.1017/CBO9780511841552

Socco, L.V. & Strobbia, C. (2004). Surface-wave method for near-surface characterization: a tutorial. *Near Surface Geophysics*, 2(4), 165-185. https://doi.org/10.3997/1873-0604.2004015

Socco, L.V., Foti, S. & Boiero, D. (2010). Surface-wave analysis for building near-surface velocity models — Established approaches and new perspectives. *Geophysics*, 75(5), 75A83-75A102. https://doi.org/10.1190/1.3479491

Stump, B.W. (1991). NUCLEAR EXPLOSION SEISMOLOGY: Verification, Source Theory, Wave Propagation and Politics. *Reviews of Geophysics*, 29, 734-742. https://doi.org/10.1002/rog.1991.29.s2.734

T. Editors of Encyclopaedia (2024). seismic wave. In *Encyclopedia Britannica*. Britannica. Retrieved May 14, 2024, from https://www.britannica.com/science/seismic-wave

TESSERAL Technologies (n.d.). Finite-difference Calculation in Tesseral. http://www.tesseral-geo.com/documentation/en/troubleshooting/WaveEquationFinite-DifferenceCalculations.pdf

Tylor-Jones, T. & Azevedo, L. (2022). The Seismic Method. In Tylor-Jones, T. & Azevedo, L. (Eds.), *A Practical Guide to Seismic Reservoir Characterization. Advances in Oil and Gas Exploration & Production* (pp. 5-32). Springer. https://doi.org/10.1007/978-3-030-99854-7_2

Virieux, J. (1986). *P-SV* wave propagation in heterogeneous media: Velocity-stress finite-difference method. *Geophysics*, 51(4), 889-901. https://doi.org/10.1190/1.1442147

Appendices

1. Numerical methods on Tesseral PRO

1.1 1D wave equation in a staggered finite differences grid

From the 1D wave equation:

$$\frac{\delta^2 U(x,t)}{\delta t^2} = b(x)\frac{\delta}{\delta x}\left(\frac{\delta \tau(x,t)}{\delta t}\right) \quad (10)$$

where $U(x,t)$ is the particle velocity, $\tau(x,t)$ corresponds to the stress, and $\frac{1}{b(x)} = \rho(x)$ is defined as the density. After integrating in time, the following equation it is obtained:

$$\frac{\delta U(x,t)}{\delta t} = b(x)\,\frac{\delta \tau(x,t)}{\delta x} \quad (11)$$

On the other side, by defining the stress as: $\tau = a(x)\frac{\delta u_y}{\delta x}$, where $\frac{\delta u_y}{\delta x}$ is defined as the strain, and $a(x) = \mu$ corresponds to the shear modulus. After differentiating both sides of the equation by the time, considering that the derivative of the particle displacement in time (u_y) is the particle velocity ($U(x,t)$), it is obtained:

$$\frac{\delta \tau(x,t)}{\delta t} = a(x)\,\frac{\delta U(x,t)}{\delta x} \quad (12)$$

What Tesseral Pro uses to solve Eqs. 11 and 12 is the combination of the 2nd order central finite difference numerical method and the concept of staggered grid. The central finite difference method uses all the adjacent points to calculate the derivative at a certain point of the grid. Mathematically:

$$f'(x) = \frac{f(x+dx) - f(x-dx)}{2 \cdot dx} \quad (13)$$

Meanwhile the concept of staggered grid is defined as a grid where the derivative of a function is defined in between the points where the function is defined. As it can be seen with Eqs. 11 and 12 it is possible to define stresses as a derivative of velocities, and vice versa. Which permits applying the concept of staggered grid to define the stress and velocity values on different positions. This way the central finite difference method can be defined as shown in Eq. 14.

$$f'(x) = \frac{f\left(x + \frac{dx}{2}\right) - f\left(x - \frac{dx}{2}\right)}{dx} \quad (14)$$

With this staggered formulation it can be seen that with the same computational power, the grid increment is dx instead of $2dx$, which means that the accuracy is doubled.

This scheme is shown in Fig. 54, where the even mesh positions correspond to the stress values, while the velocities are defined on the odd points. In this example, for not working with decimal indices, all the indices have been multiplied by 2. Meaning that the physical spacing interval between two nodes (Δx) is now defined as the distance between two odd points in the mesh.

Applying the numerical method over the coupled formulation wave equation, the following expressions are obtained, from which the values of the stress and velocity are computed at each corresponding mesh point at each time step (Δt). It is important to remark that an initial model for both velocity and stress is needed in order to solve the numerical problem.

$$\begin{cases} \dfrac{U_i^{j+1} - U_i^{j-1}}{\Delta t} = b_i \dfrac{\left(\tau_{i+1}^{j} - \tau_{i-1}^{j}\right)}{\Delta x} \rightarrow U_i^{j+1} = U_i^{j-1} + b_i \dfrac{\Delta t}{\Delta x}\left(\tau_{i+1}^{j} - \tau_{i-1}^{j}\right) \\ \dfrac{\tau_{i+1}^{j+2} - \tau_{i+1}^{j}}{\Delta t} = b_i \dfrac{\left(U_{i+2}^{j+1} - U_i^{j+1}\right)}{\Delta x} \rightarrow \tau_{i+1}^{j+2} = \tau_{i+1}^{j} + a_{i+1} \dfrac{\Delta t}{\Delta x}\left(U_{i+2}^{j+1} - U_i^{j+1}\right) \end{cases} \quad (15)$$

Where: $i = \cdots, -3, -1, 1, 3, \ldots; \; j = 1, 2, 3, \ldots$.

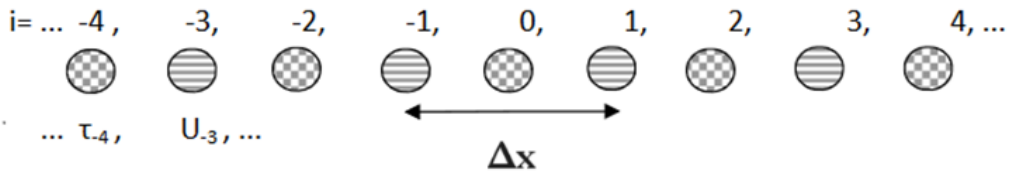

Figure 54: Schematic structure of a time step staggered grid for a 1D wave equation. Modified from TESSERAL Technologies (n.d.)

1.2 2D elastic wave equation in a staggered finite differences grid

Taking the 2D elastic wave equation, where $(\tau_{xx}, \tau_{zz}, \tau_{xz})$ is the stress tensor, (u_x, u_z) is the particle displacement, (v_x, v_z) is the particle velocity vector, $\lambda(x, z)$ and $\mu(x, z)$ are the Lamé coefficients, the following expressions are obtained (Virieux, 1986).

- $\rho \frac{\delta^2 u_x(x,t)}{\delta t^2} = \frac{\delta \tau_{xx}}{\delta x} + \frac{\delta \tau_{xz}}{\delta z} \rightarrow \rho \frac{\delta v_x(x,t)}{\delta t} = \frac{\delta \tau_{xx}}{\delta x} + \frac{\delta \tau_{xz}}{\delta z}$
- $\rho \frac{\delta^2 u_z(x,t)}{\delta t^2} = \frac{\delta \tau_{xz}}{\delta x} + \frac{\delta \tau_{zz}}{\delta z} \rightarrow \rho \frac{\delta v_z(x,t)}{\delta t} = \frac{\delta \tau_{xz}}{\delta x} + \frac{\delta \tau_{zz}}{\delta z}$
- $\tau_{xx} = (\lambda + 2\mu) \frac{\delta u_x}{\delta x} + \lambda \frac{\delta u_z}{\delta z} \rightarrow \frac{\delta \tau_{xx}}{\delta t} = (\lambda + 2\mu) \frac{\delta v_x}{\delta x} + \lambda \frac{\delta v_z}{\delta z}$ (16)
- $\tau_{zz} = (\lambda + 2\mu) \frac{\delta u_z}{\delta z} + \lambda \frac{\delta u_x}{\delta x} \rightarrow \frac{\delta \tau_{zz}}{\delta t} = (\lambda + 2\mu) \frac{\delta v_z}{\delta z} + \lambda \frac{\delta v_x}{\delta x}$
- $\tau_{xz} = \mu \left(\frac{\delta u_x}{\delta z} + \frac{\delta u_z}{\delta x} \right) \rightarrow \frac{\delta \tau_{xz}}{\delta t} = \mu \left(\frac{\delta v_x}{\delta z} + \frac{\delta v_z}{\delta x} \right)$

Proceeding equally than done for the 1D wave equation, as in this case the equation to be solved corresponds to the 2D elastic wave equation, at each time step 5 parameters should be solved. Applying again the 2nd order central finite difference, using the definition of staggered grid and taking the advantage that τ_{xx} and τ_{zz} can be solved in the same point, as they are independent between them but depend on the same parameters. This 5 can be computed at 4 different points in a 3D staggered grid. Each group of 4 points are located inside grid cubes of sides Δx, Δz and Δt, which correspond to the horizontal, vertical grid spacing and the time step, respectively.

As it can be seen in in Fig. 55, this staggered grid building permits to double the accuracy in both spatial directions and also in time without increasing the computational necessities. With this disposition, to solve the 2D elastic wave equation problem using the 2nd order central difference over a Finite difference staggered grid, the expressions in Eq. 17 need to be solved at each grid cube and time step.

- $U_{i,j}^{k+\frac{1}{2}} = U_{i,j}^{k-\frac{1}{2}} + B_{i,j}\frac{\Delta t}{\Delta x}\left(\Sigma_{i+\frac{1}{2},j}^{k} - \Sigma_{i-\frac{1}{2},j}^{k}\right) + B_{i,j}\frac{\Delta t}{\Delta z}\left(\Xi_{i+\frac{1}{2},j}^{k} - \Xi_{i-\frac{1}{2},j}^{k}\right)$
- $V_{i+\frac{1}{2},j+\frac{1}{2}}^{k+\frac{1}{2}} = V_{i+\frac{1}{2},j+\frac{1}{2}}^{k-\frac{1}{2}} + B_{i+\frac{1}{2},j+\frac{1}{2}}\frac{\Delta t}{\Delta x}\left(\Xi_{i+1,j+\frac{1}{2}}^{k} - \Xi_{i,j+\frac{1}{2}}^{k}\right) + B_{i+\frac{1}{2},j+\frac{1}{2}}\frac{\Delta t}{\Delta z}\left(T_{i+\frac{1}{2},j+1}^{k} - T_{i+\frac{1}{2},j}^{k}\right)$
- $\Sigma_{i+\frac{1}{2},j}^{k+1} = \Sigma_{i+\frac{1}{2},j}^{k} + (L+2M)_{i+\frac{1}{2},j}\frac{\Delta t}{\Delta x}\left(U_{i+1,j}^{k+\frac{1}{2}} - U_{i,j}^{k+\frac{1}{2}}\right) + L_{i+\frac{1}{2},j}\frac{\Delta t}{\Delta z}\left(V_{i,j+1}^{k+\frac{1}{2}} - V_{i,j}^{k+\frac{1}{2}}\right)$ (17)
- $T_{i+\frac{1}{2},j}^{k+1} = T_{i+\frac{1}{2},j}^{k} + (L+2M)_{i+\frac{1}{2},j}\frac{\Delta t}{\Delta z}\left(V_{i,j+1}^{k+\frac{1}{2}} - V_{i,j}^{k+\frac{1}{2}}\right) + L_{i+\frac{1}{2},j}\frac{\Delta t}{\Delta x}\left(U_{i+1,j}^{k+\frac{1}{2}} - U_{i,j}^{k+\frac{1}{2}}\right)$
- $\Xi_{i,j+\frac{1}{2}}^{k+1} = \Xi_{i,j+\frac{1}{2}}^{k} + M_{i,j+\frac{1}{2}}\frac{\Delta t}{\Delta z}\left(U_{i,j+1}^{k+\frac{1}{2}} - U_{i,j}^{k+\frac{1}{2}}\right) + M_{i,j+\frac{1}{2}}\frac{\Delta t}{\Delta x}\left(V_{i+1,j}^{k+\frac{1}{2}} - V_{i,j}^{k+\frac{1}{2}}\right)$

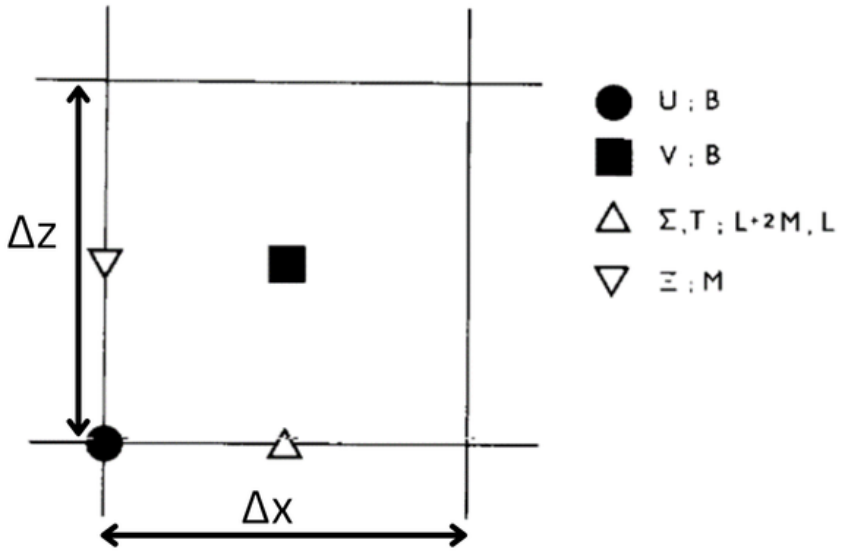

Figure 55: Medium discretisation on a staggered grid cube containing all the information of a node at a certain time step. Black filled symbols, corresponding to the velocities and density are located at the base of the cube, at a time $k\Delta z$, while white filled symbols corresponding to the Lamé coefficients and the stress values are located at half height of the cube, at a time $(k+\frac{1}{2})\Delta z$. Modified form Virieux (1986).

1.3 Stability of 2D wave equation: Von Neumann stability analysis

Even though the numerical method used is absolutely stable, finite difference method is not stable over all conditions (Quarteroni, 2016). Using a big grid spacing and time step will reduce the computational time. However, if they are too big, this leads to the creation of instabilities that will produce an incorrect final result. For that reason, a stability analysis has to be done in order to understand which the criteria are to ensure convergence of the final result.

To evaluate the stability, the Von Neumann stability analysis is performed. Starting from the 2D elastic wave equation in a homogeneous space where $\overline{x} = (x, z)$:

$$\frac{\delta^2 u_y(\overline{x}, t)}{\delta t^2} = c^2(\overline{x}, z)\left(\frac{\delta^2 u_y(\overline{x}, z, t)}{\delta \overline{x}^2}\right) \quad (18)$$

Discretising Eq. 18 in space and time:

$$\frac{u_{j,m}^{n+1} - 2u_{j,m}^{n} + u_{j,m}^{n-1}}{\Delta t^2} = c_{j,m}^2 \frac{u_{j+1,m}^{n} - 2u_{j,m}^{n} + u_{j-1,m}^{n}}{\Delta x^2} + c_{j,m}^2 \frac{u_{j,m+1}^{n} - 2u_{j,m}^{n} + u_{j,m-1}^{n}}{\Delta z^2} \quad (19)$$

Using the elastic plane wave in the exponential form: $u_y(\overline{x}, t) = A_y e^{i(\overline{k}\cdot\overline{x} - \omega t)}$, discretizing and applying it in Eq. 19.

$$A_y e^{i(kj\Delta x + km\Delta z - \omega n\Delta t)}\left[\frac{e^{i\omega\Delta t} - 2 + e^{-i\omega\Delta t}}{\Delta t^2}\right] =$$

$$c_{j,m}^2 A_y e^{i(kj\Delta x + km\Delta z - \omega n\Delta t)}\left[\frac{e^{ik\Delta x} - 2 + e^{-ik\Delta x}}{\Delta x^2} + \frac{e^{ik\Delta z} - 2 + e^{-ik\Delta z}}{\Delta z^2}\right] \quad (20)$$

Simplifying and defining: $c = \max(c_{j,m})$, as the maximum velocity:

$$\left[\frac{e^{i\omega\Delta t} - 2 + e^{-i\omega\Delta t}}{\Delta t^2}\right] = c^2\left[\frac{e^{ik\Delta x} - 2 + e^{-ik\Delta x}}{\Delta x^2} + \frac{e^{ik\Delta z} - 2 + e^{-ik\Delta z}}{\Delta z^2}\right] \quad (21)$$

Using the definition of the cosine in the exponential form:

$$\left[\frac{2\cos(\omega\Delta t) - 2}{\Delta t^2}\right] = c^2\left[\frac{2\cos(k\Delta x) - 2}{\Delta x^2} + \frac{2\cos(k\Delta z) - 2}{\Delta z^2}\right] \quad (22)$$

Taking in account the trigonometrical relation: $2 \cdot \sin^2\left(\frac{x}{2}\right) = 1 - \cos(x)$, and simplifying:

$$\sin^2\left(\omega\frac{\Delta t}{2}\right) = c^2\Delta t^2\left(\frac{\sin^2\left(k\frac{\Delta x}{2}\right)}{\Delta x^2} + \frac{\sin^2\left(k\frac{\Delta z}{2}\right)}{\Delta z^2}\right) \quad (23)$$

Taking the square root in both sides of Eq. 23 and assuming that the grid size is the same at all directions, $\Delta x = \Delta z = \Delta d$:

$$\sin\left(\omega\frac{\Delta t}{2}\right) = c\Delta t\sqrt{\left(\frac{\sin^2\left(k\frac{\Delta d}{2}\right)}{\Delta d^2} + \frac{\sin^2\left(k\frac{\Delta d}{2}\right)}{\Delta d^2}\right)} \rightarrow \sin\left(\omega\frac{\Delta t}{2}\right)$$
$$= \frac{c\Delta t}{\Delta d}\sqrt{2}\sin\left(k\frac{\Delta d}{2}\right) \quad (24)$$

As both sinusoidal functions in Eq. 24 cannot be bigger than 1, we obtain have the following stability relation derived from the Courant-Friedrichs-Lewy (CFL) condition:

$$\sqrt{2}\frac{c\Delta t}{\Delta d} \leq 1 \rightarrow G = \frac{\Delta d}{\Delta t} \geq \sqrt{2}c \rightarrow \Delta t \leq \frac{\Delta d}{\sqrt{2}\,c} \quad (25)$$

The derived condition controls the range of values of the grid space and the time together with the condition presented by Mufti (1990) that states the condition for the maximum grid spacing to avoid numerical dispersion:

$$\Delta d \leq \frac{c_{min}}{w\,f_{max}} \quad (26)$$

Where, c_{min} is the minimum velocity in the model, f_{max} is the maximum frequency in the source wavelet, and w, which in general is defined as $w \geq 10$, corresponds to the number of wavelength samples for the maximum frequency.

If the same study is done for the 3D case, the only condition changing is the relation derived from the CFL condition (Eq. 25) which becomes (Lines et al., 1998):

$$G = \frac{\Delta d}{\Delta t} \geq \sqrt{3}c \rightarrow \Delta t \leq \frac{\Delta d}{\sqrt{3}\,c} \quad (27)$$

Acknowledgments

I would like to take a moment to thank everyone who has contributed and supported me throughout the process of writing this master thesis and in general during all my entire academic journey.

First and foremost, I would like to express my deepest appreciation to my supervisor, Dott.ssa Ilaria Barone. Thank you for encouraging me to pursue this topic for my master thesis and for your unwavering support, supervision and guidance of my work during the several months I worked on the thesis. Words cannot express my gratitude to my co-supervisor, Dott. Claudio Strobbia, for all his guidance, patience and invaluable assistance in creating and simulating all the different models. Your extensive knowledge of surface waves was crucial in solving all the challenges I faced and to interpret all the results I obtained. Additionally, I share the same level of gratefulness to you as the CEO of realtimeseismic (RTS) for allowing me to work at during this time in the company's headquarters in Pau, France. Access to RTS's internal tools and software licenses significantly enhanced my research.

I would like to extend my sincere thanks to all the employees and interns on RTS, especially those in Pau, and also those in Australia and the UK. Your invaluable help with any questions or issues I had, alongside with your support in helping me adapt to the company and the country, was greatly appreciated.

I would like to thank the teachers and classmates of the Department of Geosciences of the University of Padova. Your knowledge and support have been instrumental in my development as a geophysicist. Without all of you my life this year in a half studying abroad in Italy would not be as wonderful and enriching experience as it has been.

Further, I would like to recognise all my family for their unconditional moral and economical support though my life, always being there during both the good and the challenging moments.

Last but not least, I genuinely thank all my friends, classmates, and anyone who has shared part of this journey with me. Your companionship, patience, encouragement, and all the good times we have shared helped me grow as a human being and becoming the person I am today.

To all of you, I cannot say anything more than thank you!

Roger Puiggròs Valentines

16th July, 2024 (Cervera, Spain)